PRESSURE FIELD MEASUREMENTS IN A HELICAL COIL STEAM GENERATOR MODEL USING PRESSURE SENSITIVE PAINT

A Thesis

by

GARLAND ALEC PORTER

Submitted to the Office of Graduate and Professional Studies of
Texas A&M University
in partial fulfillment of the requirements for the degree of

MASTER OF SCIENCE

Chair of Committee,	Yassin A. Hassan
Committee Members,	Victor Ugaz
	Rodolfo Vaghetto
	Duy T. Nguyen
Head of Department,	Michael Nastasi

May 2020

Major Subject: Nuclear Engineering

ABSTRACT

Helical coil heat exchangers are types of tube and shell heat exchangers that have been implemented in processing plants, oil and gas, and refrigeration. Currently several designs have been proposed for next generation nuclear power plant designs, such as small modular reactors, high temperature reactors, and molten salt reactors. Helical coil designs are under consideration due to their compact designs and superior heat transfer efficiencies when compared to straight pipe designs. Designs are characterized by the geometry of the tube bundle, which is described as either in-line (square) or staggered (triangular). This study focuses on a helical coil design that has interlacing tube bundles, which causes the tube bundle geometry to shift between in-line and staggered. Cross sectional geometries have been previously correlated to pressure drop, friction factor, and heat transfer efficiencies depending on parameters such as pitch, tube sizing, and spacing between tubes. Additionally, tube bundles with staggered arrangements are known to cause additional disruptions in the flow which can lead to more turbulence between the tubes. Studying the effects of the tube bundle arrangement on shell side flow has typically been done by measuring pressure drops and temperature changes using pressure transducers and thermocouples respectively. This study uses the pressure sensitive paint technique to analyze pressure distributions on the surface of the tubes, and validates measurements by comparing them to static pressure transducers. Pressure sensitive paint is a technique commonly used in aerospace research studies. This

technique utilizes a luminescent dye that reacts to the partial pressure of oxygen, allowing full field pressure measurements on an objects surface. Experiments using pressure sensitive paint were performed on a helical coil steam generator model at Re 4000, 6000, 8500, and 11600. Two different paint formulations were used to develop instantaneous and average pressure distributions on the surface of the tubes. This study outlines the development of a wind tunnel containing a helical coil steam generator model, and presents full field pressure measurements on the surface of tubes. Measurements show that the interlacing tube bundle geometry causes significant turbulence on tubes in the developed region of flow, but the pressure distributions are dependent upon tube location. This means adjacent tubes in the same bundle were found to not share similar pressure distribution patterns.

ACKNOWLEDGEMENTS

I would like to thank my committee chair, Dr. Yassin A. Hassan for his support, patience, and guidance throughout the course of my research. I would like to thank my committee members Dr. Rodolfo Vaghetto and Dr. Thien Nguyen for their support and advice throughout my years working at the lab. I would like to thank my committee member Dr. Victor Ugaz for providing an outside viewpoint and supporting my research. Outside of my committee, I would like to thank Dr. Saya Lee for providing his help and advice, which has helped me through some of the most difficult parts of my research. I would also like to thank Marilyn Delgado, without your help I would still be working on my first journal publication.

I would also like to thank Michael S. Gorman and Brent Hollrah, for supporting me through difficult times. Finally, I would like to thank my parents and sisters for being my greatest support in life and for motivating me to succeed.

CONTRIBUTORS AND FUNDING SOURCES

This work was supported by a dissertation committee consisting of Professor Yassin A. Hassan, as an advisor, and Dr. Rodolfo Vaghetto and Dr. Duy Thien Nguyen of the Department of Nuclear Engineering and Dr. Victor Ugaz of the Department of Chemical Engineering. This work was partially financially supported from Argonne National Laboratory through the Nuclear Energy Advanced Modeling and Simulation (NEAMS) program of the Department of Energy (DOE). All work for the thesis was completed independently by the student.

NOMENCLATURE

a	Transverse pitch ratio
$A(T)$	Stern-Volmer calibration coefficient
b	Lateral pitch ratio
$B(T)$	Stern-Volmer calibration coefficient
C_p	Pressure coefficient
D	Diameter of rod
I	Intensity of luminescence
I_0	Intensity of luminescence without air flow
N	Total number of pixels on the surface of the rod
P	Pressure
$P_{i,j}$	Pressure at pixel with coordinate location (i,j)
P_{ref}	Ambient pressure
$\bar{P}$	Average surface pressure on the rod
P_θ	Mean pressure at specific angle
$P_{\theta max}$	Mean pressure at stagnation point
Re	Reynolds number
R_{PSP}	Residual value
S_T	Transverse pitch
S_L	Lateral pitch
U_g	Gap velocity

υ Kinematic viscosity of air

V_i Average inlet velocity

TABLE OF CONTENTS

Page

LIST OF FIGURES

Page

LIST OF TABLES

CHAPTER I

INTRODUCTION

The Helical Coil Steam Generator

Nuclear power plants have used a variety of heat exchanger designs over the last fifty years to transfer energy from the primary coolant loop to the secondary coolant loop. The purpose of these heat exchangers is to prevent accidental release of radioactive coolant into the atmosphere, while transferring energy to the turbines as efficiently as possible. As new heat exchanger designs are being proposed and implemented, it is increasingly important to improve experimental data since these designs are becoming increasingly complex and have unpredictable fluid characteristics. Predicting the pressure distribution within a heat exchanger is fundamental to improving design, increasing efficiency, and ultimately determining pumping power required. Recently, helical coil steam generators (HCSG) have been proposed in next generation SMR reactor designs, such as CAREM-25, IRIS, SMART, UNITHERM, NuScale, ACPR50S, HTMR-100, and 4S [1].

HCSG's are a type of tube and shell heat exchangers that are being considered as replacements for traditional straight pipe heat exchangers. They offer improved heat transfer efficiencies, and are more volumetrically compact when compared to straight pipe heat exchanger designs [2]. Additionally, the helical design allows the tubes ample room to expand when subjected to high thermal stresses. Figure 1 shows what a proposed HCSG design would appear as within a reactor core configuration.

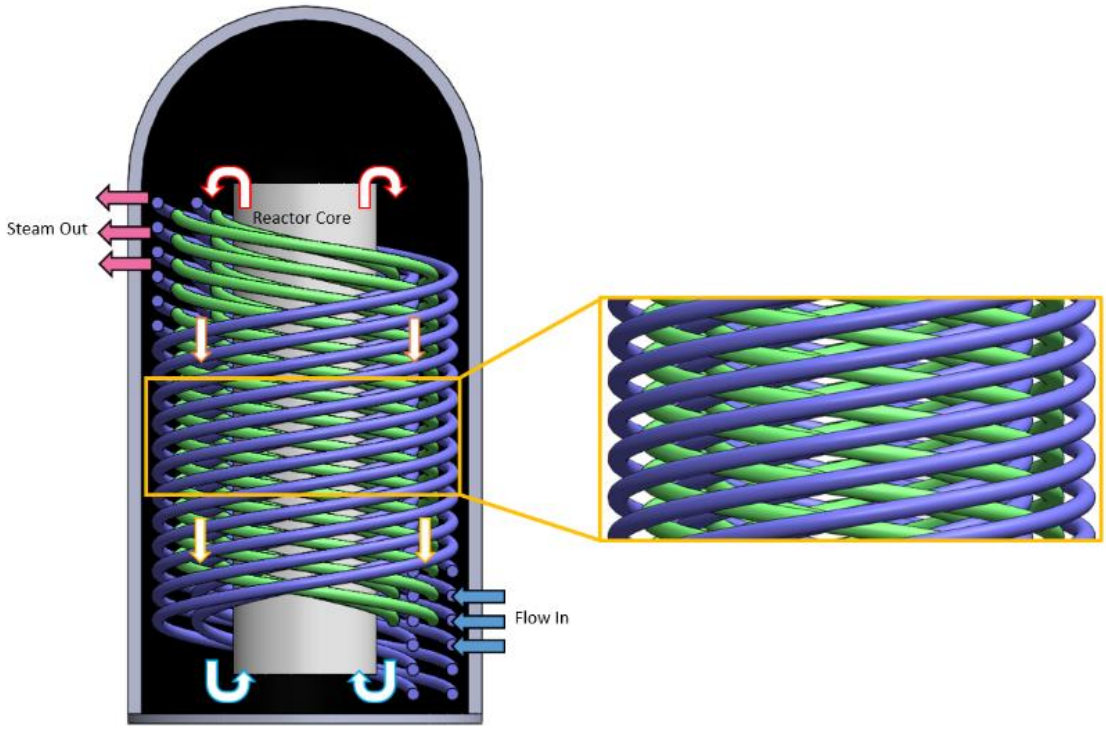

Figure 1. A Helical Coil Steam Generator (HCSG) within a reactor core

Tube and shell heat exchangers have a primary fluid flowing through a shell that passes over and transfers heat to tubes inside of the shell. The flow within the tubes can be circulated with a pump, or in some cases circulated naturally, if converted into a gas. In the case of HCSGs, the tubes are curved helically inside the shell, and are subjected to cross-flow. Typically, there are multiple concentric layers of tubes. This is what is known as the tube bundle, and the cross section between tube layers is often studied to develop correlations for pressure drop, friction factor, and heat transfer efficiency [3-6]. Heat exchangers are studied based on their characteristics, which are defined by their

flow arrangement and geometry. The flow arrangement is determined by the direction of fluid flow in the shell relative to fluid flow in the tube. In the case of HCSG's the fluids are in cross-flow which provides more efficiency than parallel-flow and counter-flow. The important geometric considerations for HCSGs are the size and cross sections of the tube bundle within the heat exchanger. The cross-section between tube bundles is typically referenced as either a staggered or an inline geometrical arrangement. A staggered cross section means the tube layers form triangular cross sections, whereas an inline cross section means the tube layers are in a square formation. Figure 2 illustrates the difference between staggered and inline tube bundles below.

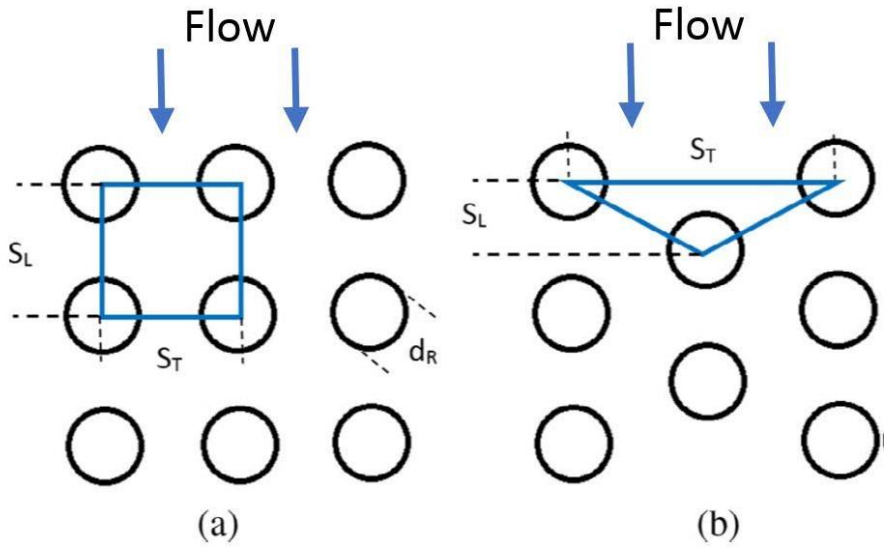

Figure 2. Two most common tube bundle configurations, (a) in-line cross section and (b) staggered cross section

HCSGs are also characterized by the pitch of their tube bundles. The pitch describes the number of times a rod coils in a given height. The pitch of the entire tube bundle is generally the same for all the layers of tubes, although an exception to this would be in cases of certain designs, such as the model HCSG employed in this study. The model HCSG used in this study has an interlacing tube bundle, which means the pitch alternates between tube layers. This causes the cross section to constantly change depending on location. This design is typically used in HCSG designs proposed for use in the nuclear industry.

As mentioned previously, the cross section between tube layers can be inline or staggered. The cross section can also be described by pitch ratios. There are two pitch ratios that can be used to determine a tube bundles cross sectional orientation, the transverse pitch ratio, *a*, and the lateral pitch ratio, *b*. The transverse pitch ratio is the ratio of the transverse pitch, S_T, to the diameter of the tube, D, and the lateral pitch ratio is the ratio of the lateral pitch, S_L, to the diameter of the tube, D. Inline arrangements imply that the lateral pitch ratio and transverse pitch ratio are equivalent i.e. $a = b$, where staggered arrangements can be represented by a relationship such as $a = 2b/\sqrt{3}$ for an equilateral tube arrangement [7]. Figure 3 shows where the lateral and transverse pitch are located.

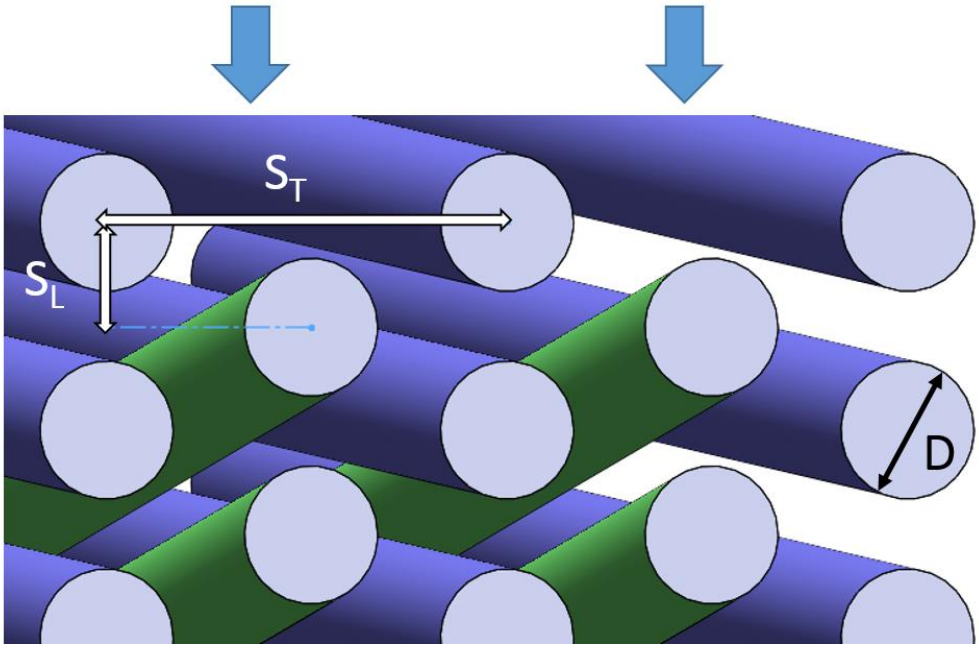

Figure 3. Lateral and transverse pitch graphical representation

The model HCSG used in this study has alternating pitches in each concentric layer of tubes, this results in a changing cross section between the tubes. The transverse pitch ratio remains constant throughout the entire test section, but the lateral pitch ratio changes depending on the location. The model HCSG that was built for this study is shown below in Figure 4.

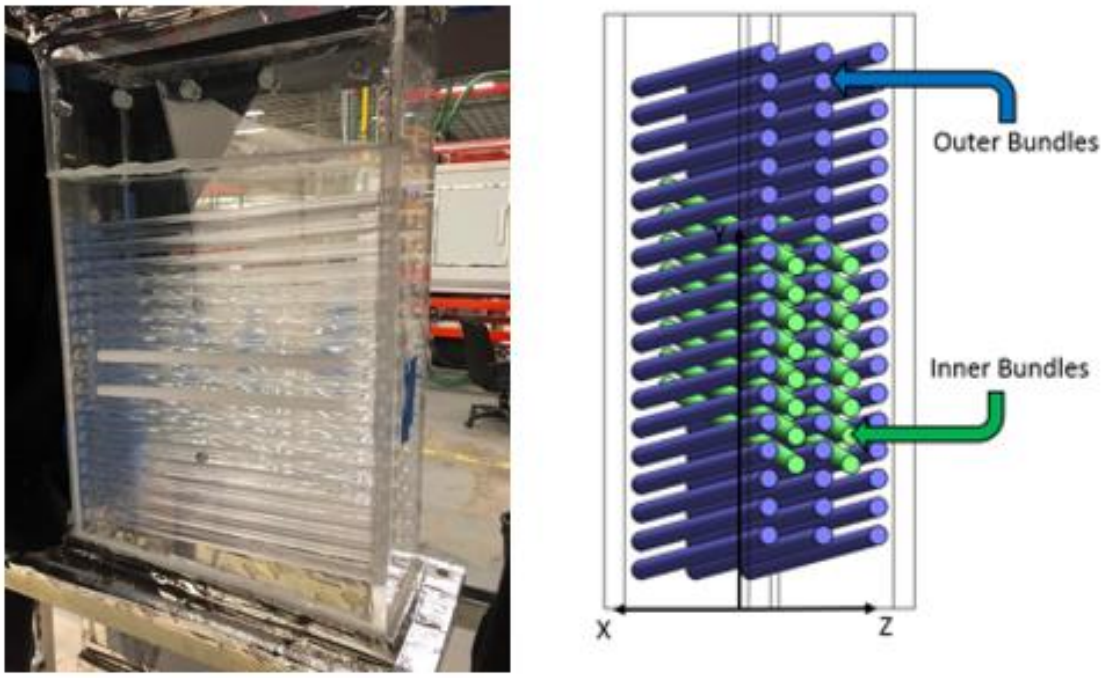

Figure 4. Model HCSG and CAD model of the test section.

HCSG's are currently being proposed in Generation IV nuclear power plant designs, including small modular reactors (SMR), which include high temperature reactors, sodium-cooled fast reactors, and molten salt reactors [8-10]. HCSG designs have previously been implemented by several other industries including processing plants, oil and gas, and refrigeration [11-13]. However, comparison between usage in the nuclear industry and other industries is often irrelevant, due to the extreme operating conditions present in a nuclear power plant. This has raised concerns for safety when operating with HCSGs, due to the size of the tube bundles and how they will react to the external stresses applied by the cross-flow [14]. External stresses applied by the flow onto the tubes is thought to be due to several effects, including vibrations caused by the

pumps and flow phenomena. Specifically, vortex shedding, a flow phenomenon known to occur within heat exchangers containing tube bundles, is known to be one of the causes of significant vibrations on the surface of the tube. Vortex shedding occurs when eddies form below the tubes, detach, enter the stream between tube bundles, and reform periodically [15]. The vortices formed exert pressure on the surfaces they form between, and the process of the vortex shedding into the fluid stream can cause a low pressure zone to occur. The entire process can occur as fast as 24 Hz [16]. Due to the speed of this phenomena, static pressure transducers cannot capture the rapid pressure fluctuations, and provide limited information on where the pressure changes are occurring. Subsequently, more advanced measurement techniques need to be employed.

In aerospace research, a technique called pressure sensitive paint (PSP) has been widely implemented for studies of pressure fields over complex geometries. Prior to the usage of this technique, the preferred method of determining pressure fields was to use a large number of pressure transducers placed on top of the model being tested. This caused significant uncertainty and errors in readings, since the pressure transducers interfered with air flow, and pressures between transducers could only be estimated by interpolation. PSP is a non-intrusive, distributed technique capable of discerning the entire pressure field over an object's surface without obstruction.

Since PSP can provide measurements of the surface pressure, it can be compared to previous research done on surface pressure distributions. A multitude of studies have been performed to determine pressure distributions on the surface of tubes in both staggered and inline arrangements [17-25]. These studies range from measurements at

Re = 8×10^3 to 5×10^6 and use traditional pressure transducers to gather the surface pressure on the tubes within the bundles. To provide interpretable data from experiments, each study chose to present pressure data through the pressure coefficient, C_p, which is a non-dimensional representation of the mean pressure presented circumferentially around the rod. Equation 1 below gives the equation for C_p.

$$C_p = 1 - \frac{P_{\theta \max} - P_\theta}{\frac{1}{2}\rho U_g^2} \qquad \text{Eq. 1}$$

Where $P_{\theta \max}$ refers to mean pressure at stagnation point, P_θ is the mean pressure at specific angle (relative to stagnation point), U is the gap velocity, and ρ is the density. Figure X below shows the stagnation point location and angles relative to the direction of air flow in the test model.

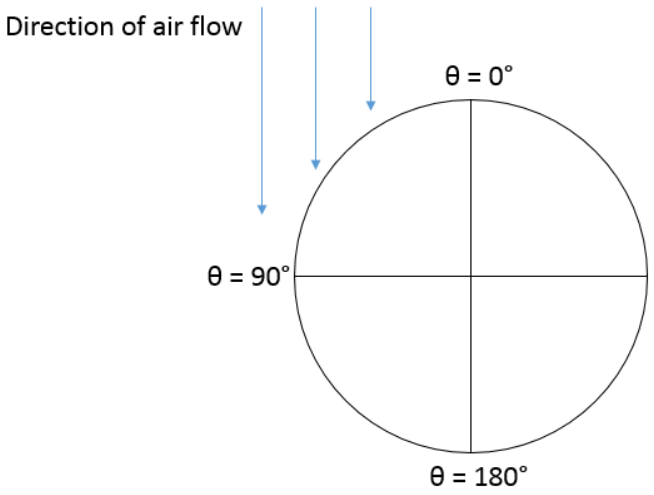

Figure 5. Angles represented on a tube within the model

Pressure Sensitive Paint

PSP was first formulated and implemented in the early 1980's, and has seen growing usage since then [26]. Initially, researchers found dyes with fluorescent properties that reacted to oxygen, and then used this discovery to discern the pressure on the surface of the dye. The fluorescent dye in the paint depends on the partial pressure of oxygen, this is also known as oxygen quenching. Oxygen quenching is a physical process that occurs when excited molecules are able to interact with oxygen molecules to return to their ground states. The alternative decay to ground state when oxygen quenching is present, is through emission of a photon. This implies that when oxygen quenching is occurring on excited molecules, that there is a relationship between the intensity of luminescence and the partial pressure of oxygen on the surface, since oxygen quenching occurs at a higher rate when pressure is increased [27]. Figure 6 illustrates the process of oxygen quenching.

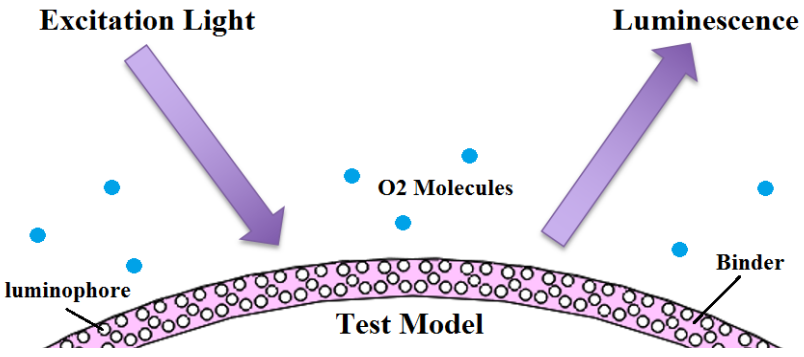

Figure 6. Oxygen quenching process

Estimating the pressure on the surface of PSP can be done using the Stern-Volmer equation. The Stern-Volmer equation is applied at known pressures to determine calibration coefficients, which can then be used to determine pressures within the range of the calibration. Stern-Volmer equation is given below as Eq. 2.

$$\frac{I_0}{I} = A(T) + B(T) * \frac{P}{\mathrm{P_{ref}}} \qquad \text{Eq. 2}$$

Where I_0 is the intensity of luminescence at ambient pressure and temperature, I is the intensity of luminescence with a quencher, P is the pressure, P_{ref} is the pressure at ambient pressure, A is the Stern-Volmer calibration coefficient for efficiency of paint sensitivity, and B is the Stern-Volmer calibration coefficient for paint sensitivity. The coefficient B ranges from 0.3 to almost 1.0 for the most sensitive PSP formulations [28].

PSP techniques uses an LED light source to excite photoluminescent molecules, and then captures the light emission with a CCD or CMOS camera. The camera that is chosen for experiments must have a matching quantum efficiency to the paint chosen, or significant portions of light emissions will be lost when captured. PSP can only be used on test models subjected to oxygen, so air is typically chosen as the working fluid in any facility that applies this technique. Once captured, PSP images are analyzed by comparison of a wind-off frame (no wind forces applied) to wind-on frames, utilizing the Stern-Volmer relation to discern pressures. PSP is a new technique, and so further advancements in paint formulations and analysis methods will lead to improved data collection. Prior to the mid 2000's binary formulations used were composed of a simple

polymer binder and a luminescent molecule. Current technology allows for accurate analysis of experiments ranging from low speed experimental flow to complex geometries operating in Mach speeds [29, 30]. A comprehensive, detailed history of PSP is outlined by Liu and Sullivan [27]. PSP techniques have gone through several iterations of development. Recent improvements have resulted in porous paint formulations, which have increased the time resolution of measurements from the order of seconds to microseconds [31]. This improvement decreases PSP response time and provides enough speed to capture flow phenomena that occurs rapidly. An application of this would be measurement of pressures coinciding with vortex shedding. As mentioned previously, this flow phenomenon is being studied for its vibrational effects on the surface of tubes. It may also be related to the improved heat transfer efficiencies in HCSG designs. Developing a relationship between pressure fields and vortex shedding frequencies could lead to increased safety or heat transfer in future designs. The purpose of this study was to develop a facility that utilizes PSP within a model HCSG, and to present pressure measurements compared to pressure transducer readings using two formulations of PSP with different response times.

CHAPTER II

DESIGN AND CONSTRUCTION OF THE TEST FACILITY

Design Aspects

The experimental test facility is designed with the purpose of emulating a sectioned cut out of a HCSG. HCSG designs vary in scale. Proposed designs have included cores wrapped in their entirety by a single once-through HCSG, and cores that are surrounded by several separated HCSG bundles [9, 32]. While an HCSG uses tubes for the secondary flow, the test sections developed use solid rods, therefore the terms tube and rod will be used interchangeably. Prior to the development of the experimental test facility used in this study, two other facilities were designed and constructed - one with a curved two-rod bundle, and one with a curved five-rod bundle. This study focuses on a test section that was designed as a straight rod adaption to the curved five-rod bundle facility, and it was based on matching the inlet area of that test section.

The curved five-rod bundle facility is a 24° section of an HCSG designed with 5 concentric interlacing tube bundles. The helical body diameter of the test section is 2.02 m, and the helix-to-tube ratio is 127.2. The outer-most and center tube bundles have 18 tubes with pitches of 0.43 m, and the two inside tube bundles have 9 tubes with pitches of -1.0 m. The lateral pitch changes based upon location and the transverse pitch is 41.5 mm. The design parameters of the test section were based upon numbers found in previous literature and proposals [33]. Figure 7 illustrates how a straight model is developed from the helical coil.

Geometric parameters such as pitch, helical diameter, and helix-to-tube ratio do not adequately describe a straight test section design. Converting the curved five-rod bundle to a straight five-rod bundle was done by ensuring the inlet area and tube bundle dimensions were equivalent. Both the curved five-rod and straight five-rod test sections share the same total inlet area of 0.05 m^2. The rods possess a diameter of 15.9 mm, which is similar to other proposed HCSG designs [32]. The outer-most rods are angled at an inclination of 0.07 rad or 4° upward from left to right, and the inner bundles are angled at inclination 0.16 rad or 9° downward from left to right. The orientation of the rods is shown more clearly in Figure 8 below.

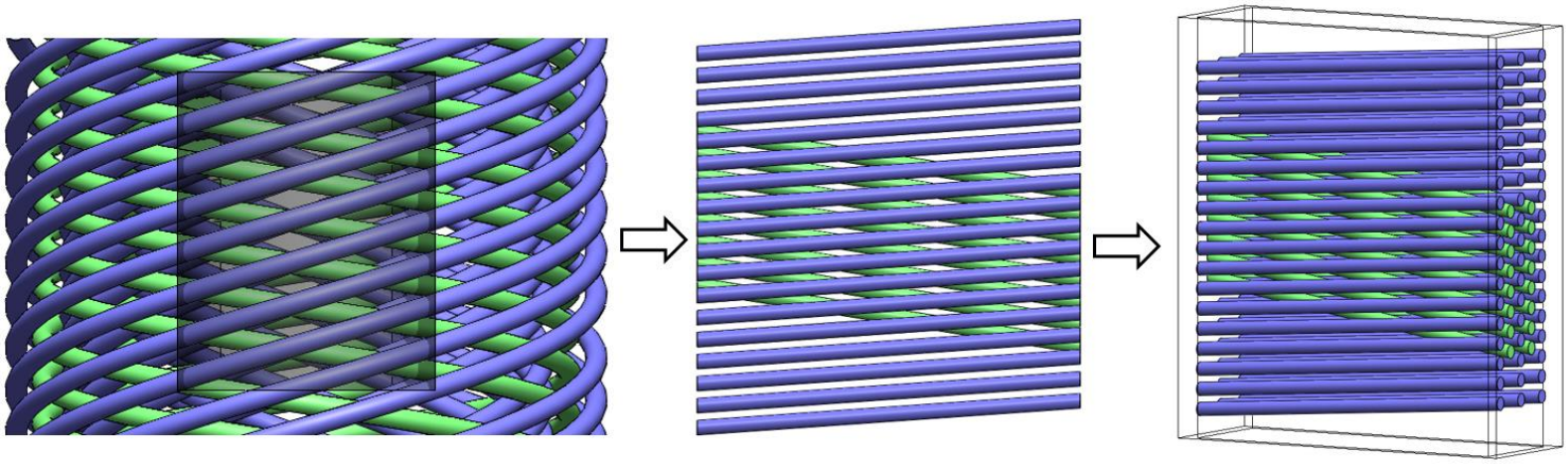

Figure 7. Development of the test section used in this study

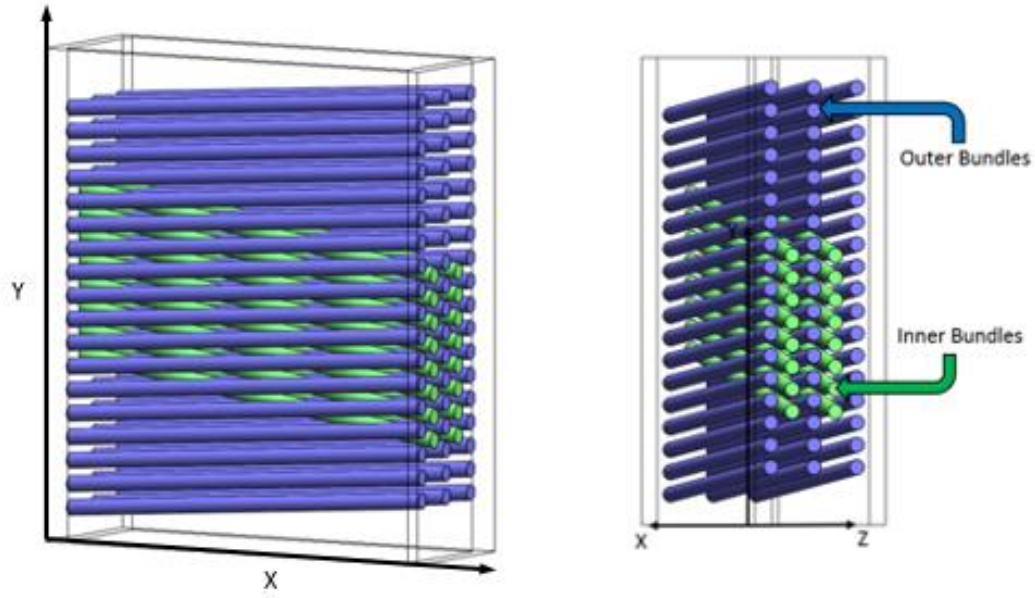

Figure 8. CAD model of straight five-rod test section

The test section is designed with neither an in-line nor a staggered cross section, since recent design proposals do not have uniformly staggered or in-line cross sections. The tube bundles are interlacing, which causes the cross section to shift between in-line and staggered depending on the location within the test section. The straight five-rod test section has a constant transverse pitch ratio of 2.98, and a lateral pitch ratio that changes from 0.74 to 1.5 depending on location.

The facility is designed to measure pressure on the surface of the rods, with the ultimate goal of studying the effects of the geometry of the interlacing tubes on the surface pressure field. The objective of this study is to analyze shell-side flow on the

surface of rods, therefore secondary flow is not considered. Important considerations for the design of the test facility and test section were a uniform inlet velocity, optical clarity in order to capture images inside of the test section, and a blower that could provide the velocity necessary to gather differentiable measurements.

Construction

Construction of the facility began with fabrication of a test section. Previous test sections had been manufactured by external sources. Outsourcing production is costly, and the five-rod curved bundled arrived heavily damaged, requiring significant in-house modifications before it was ready for experiments. This led to the decision to produce the five-rod straight bundle in-house, both to save money and to ensure a quality build.

The test section was initially designed and drawn in SolidWorks. The dimensions for the inlet were determined to be 44.45 cm length by 11.43 cm width, which matches the area of the inlet for the five-rod curved bundle. Acrylic sheets with thickness 1.27 cm were ordered along with solid acrylic rods of diameter 15.9 mm. Solid acrylic rods were ordered since secondary flow was not a consideration for design. Several hollow acrylic rods were also ordered for the purpose of using instrumentation within them after the test section was constructed.

Initially, two sets of side walls were constructed. The side walls were acrylic sheets modified to hold the rods in place. Side walls were constructed by marking the acrylic sheets with rod locations, and using a mill to drill angled holes in the marked spots. The test section was designed to be fully sealed, requiring removal of the seals to replace any components within the test section, but enabling fluid testing. Construction

of this proved problematic, as aligning the two side walls with the rods already loosely in place proved to require a more precise method than a clamp and basic tools. While this process was being resolved, Figure 9 shows the rods within one side wall.

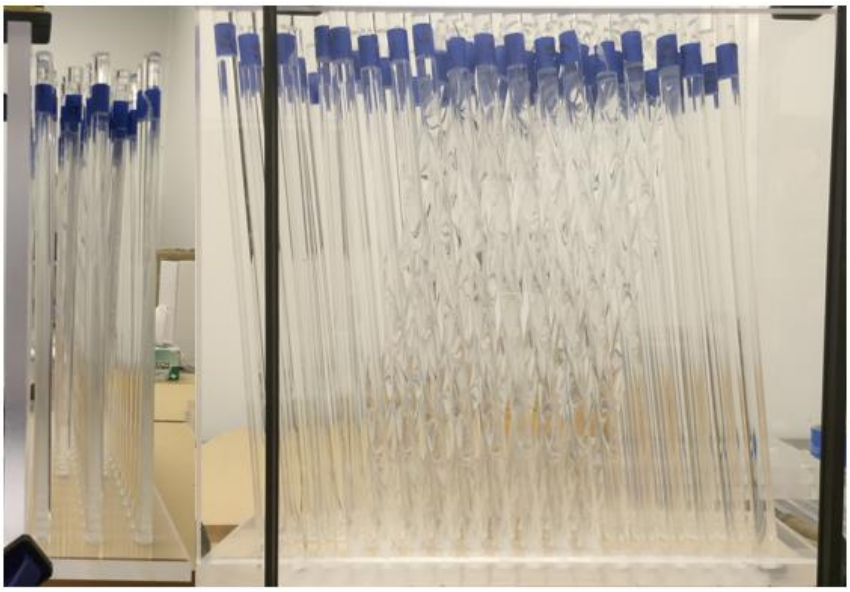

Figure 9. Rods loosely placed into sidewall

There were small errors in the diameters of each hole and the depths the holes were drilled by, resulting in the rods failing to align to both side walls simultaneously. This was later fixed for a future experiment by using a wax mold to hold the rods as both side walls were aligned. However, since this study was only going to use air, the rods were instead made to be fully removable through one side wall. Another side wall was then fabricated, and was made with thickness of 0.64 cm, with holes being drilled completely through. This enabled rods to be inserted through the side wall before

insertion into the other, ensuring a smooth fit. This also simplified the process of removing, painting, and reinserting new rods.

The wind tunnel test facility went through several different design phases. The first design utilized a suspended blower that dropped directly into the test section as seen in Figure 10.

Figure 10. Initial wind tunnel design

The purpose of the suspended blower was to save energy and prevent pressure loss from forcing the wind to rise before dropping into the test section. An aluminum frame was constructed to provide a stable base for the blower to rest on, and provided a resting angle that let the blower lead directly into the test section. The blower was lifted by a crane and fitted onto the frame, but the blower had an electrical malfunction that caused it to fail. The cause of the electrical function is still unknown, but it was possibly caused by damage to the blower from lifting it and placing it with a crane, or it could

have simply been due to the age of the blower. This resulted in a reconsideration of where the blower should be placed.

Figure 11. New blower used with aluminum duct to reach inlet

In the revised design, the test section was placed 1.5 m above the ground, and the new blower was rested upon a shock-absorbing pad placed on the ground. Figure 11 depicts the new blower. The tunnel consisted of aluminum ducts and insulation foams with flow separators and meshes placed inside the insulation foam. The flow separators were placed in the bend leading downwards into the test section as seen in Figure 12. The mesh was a 3.81 cm thick plastic honeycomb placed in a chamber directly before

the inlet. The wind tunnel, meshes, and flow straighteners were designed by the Mehta and Bradshaw's guidelines for low speed velocity experiments [34].

Figure 12. Honeycomb placement inside wind tunnel

A couple issues arose when construction the facility, one of them was caused by the aluminum duct swaying when the blower was turned on. This caused the duct to tear off from the blower and the remainder of the facility. This was solved by constructing wooden frames to hold the duct in place. Additionally, a wooden outlet, shown in Figure

13, was constructed at the blower outlet to help fasten the aluminum duct, as the previous outlet material burst from too much pressure.

Figure 13. Wooden outlet connected to blower and aluminum duct

The other issue occurring was a number of small leaks occurring through the insulation foam. The leaks were found by running the blower at high speeds and patched using duct tape. The final design for the wind tunnel used originally is shown in Figure 14.

Figure 14. Wind tunnel design used with BinaryFIB experiments

The facility was later redesigned to increase wind speeds at the inlet. The aluminum duct was removed and the blower was placed on top of a pallet of cinder

blocks. The height of the blower was raised 3 ft. The distance between the blower and the test section was also reduced. The insulation foam was still used as the bridge between the blower and the test section. The redesigned test facility is shown in Figure 15.

Figure 15. Redesigned wind tunnel used with TurboFIB experiments

The test section is housed within an aluminum frame. The frame accommodates for several additions required for PSP experiments. On the back end and sides of the frame are hooks placed to hold a laser sheet. The laser sheet is used to prevent UV light

from escaping the facility and interfering with other facilities. On the front of the frame, an aluminum breadboard was placed. The aluminum breadboard holds the cameras and UV lights, and is fastened securely to the frame. Additionally, a table was placed next to the frame, and holds the remainder of the testing equipment including the DAQ, hot film anemometer, and computer systems. Further images and details regarding setup of PSP experiments are located in Chapter 3.

CHAPTER III
EXPERIMENTAL METHOD

Calibrations

PSP experiments began with preliminary testing to help understand paint functionality and ensure a working method when used in the facility. Afterwards, calibration experiments were performed to determine accuracy and optimal application conditions for the paint. After calibration experiments concluded, the paint was used for experiments within the model HCSG. Initial applications of paint resulted in several failed tests due to over-spraying/under-spraying. Paint coats will apply poorly when sprayed as a wet coat, which causes the paint to drip or adhere unevenly.

Proper application of the paint is done by spraying cross coats using either a pressurized air brush or spray paint can. Cross coats are simply coats that are applied perpendicular to each other. Cross coats are used to ensure the most uniform application of paint possible. Typically, the object is first painted with 7 to 9 cross coats (roughly 28 to 36 μm) of base coat. Base coat is used to ensure proper adhesion of the PSP later. The PSP is then also applied with 7 to 9 cross coats. Painting with PSP is identical to using spray paint or an air brush with other paints. Coats are sprayed on lightly from at least a 12 inches or 30 cm away from the surface. For all the experiments presented, paint was applied using an air brush attached to a compressor. The air brush used a pressure regulator which set the application pressure to 10 psi.

Initial tests were basic and consisted of a 2” x 2” painted piece of acrylic that was sprayed by a compressed air can during image capturing. An image of the initial test is

shown below in Figure 16. The acrylic test piece was subjected to UV light at 410-nm, and was placed in a dark room to prevent background lighting. The emission spectra of BinaryFIB is shown below in Figure 17.

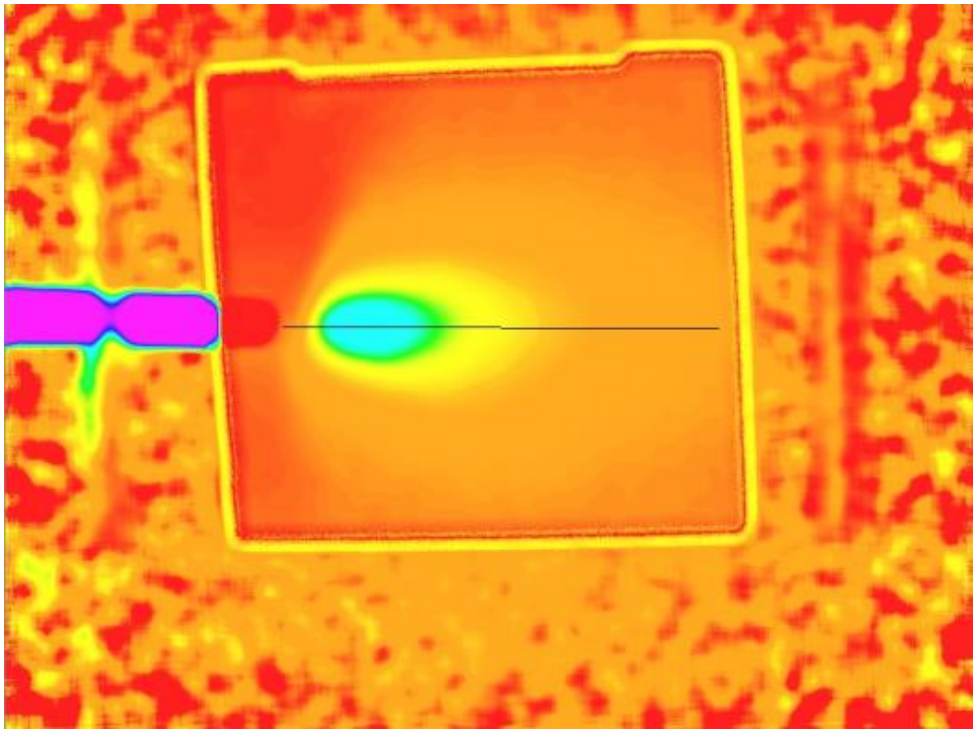

Figure 16. Preliminary PSP test on a small test piece

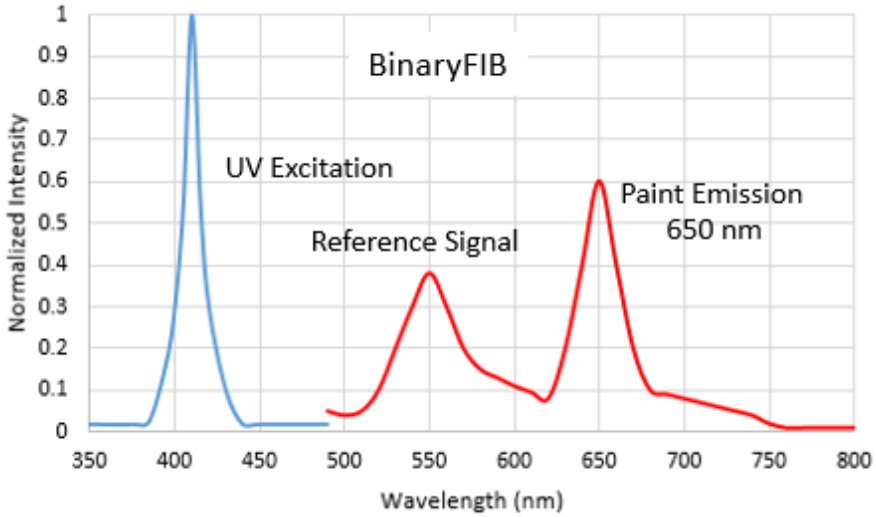

Figure 17. Emission spectra of BinaryFIB

As seen in Figure 16, there were background readings all around the image. OMSLite, the program that was used for determination of pressure fields, was found to have a dysfunctional background subtraction code. Subsequent tests used images that had their background subtracted beforehand using other programs such as ImageJ. Background subtractions were performed by removing areas between the rods completely. Pressure readings were also incorrect on the image. This was due to user error though, OMSLite requires formulation specific paint calibration coefficients to be manually input, which was misunderstood at the time of this test.

There are two types of calibration tests needed for experiments using PSP, “a-priori” and “in-situ” calibrations. A-priori calibrations are used to calibrate the pressure measurements by varying temperature and pressure. In-situ calibrations are used to calibrate PSP readings on a specific model under specific conditions by comparing

measurements to pressure taps. Additional calibrations were also done to determine paint thickness effects before application of PSP within the model HCSG.

The a-priori and paint thickness calibrations were performed concurrently. The calibrations were performed by placing painted rods into an acrylic box. The box was sealed shut with epoxy and was connected to an air compressor and a static pressure transducer. Each rod was painted with a varying thickness of both base coat and PSP, the bottom rod was painted with 5 cross coats (~40 μm), the center rod was painted with 7 cross coats (~60 μm), and the top rod was painted with 9 cross coats (~75 μm). Paint thicknesses were measured using a Mitutoyo micrometer (uncertainty of ± 6.9 μm). Experimental setup and an experimental wind-on frame are shown below in Figures 18. The paint formulation used in these experiments was BinaryFIB (ISSI Inc.).

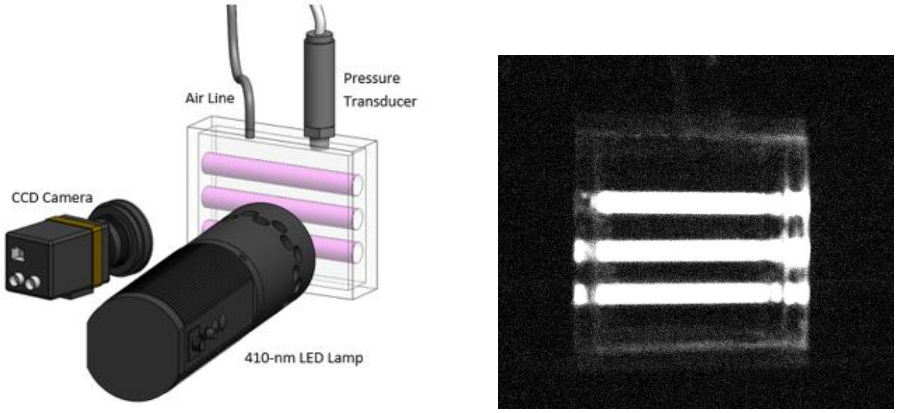

Figure 18. A-priori calibration experimental setup and wind-on frame.

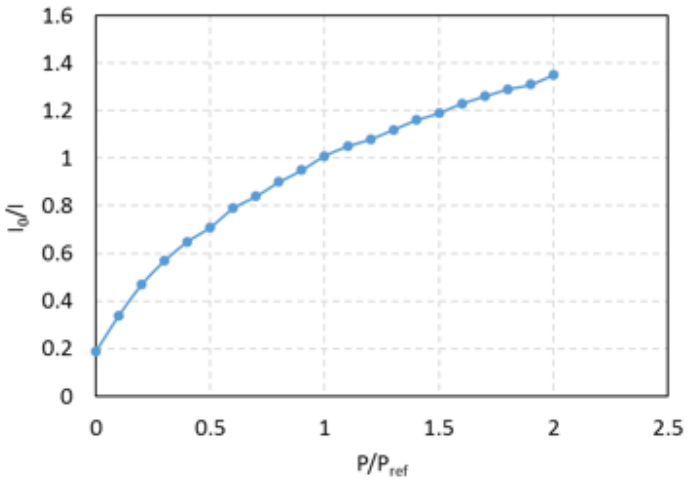

Figure 19. BinaryFIB paint intensity to pressure calibration curve

The in-situ calibration was performed after the facility was constructed. In-situ calibrations are regularly done on the models subjected to the exact same conditions as they are during experimental testing. The only difference between the models in the in-situ calibration and the experimental testing is the presence of pressure taps. In the case of this experiment, placing pressure taps on the rods during operation was infeasible. This is due to lack of space and diameter of the rods. Placing pressure taps on the rods would have interfered with flow largely, and they were too large to place inside of the rods. Another method was attempted before performing an in-situ calibration on a model outside of the facility. Dynamic pressure transducers (DPT's) were placed inside the rods during experiments, and data was extracted from them in an attempt to perform an in-situ calibration. Figure 20 shows how the DPT's were inserted into the rods.

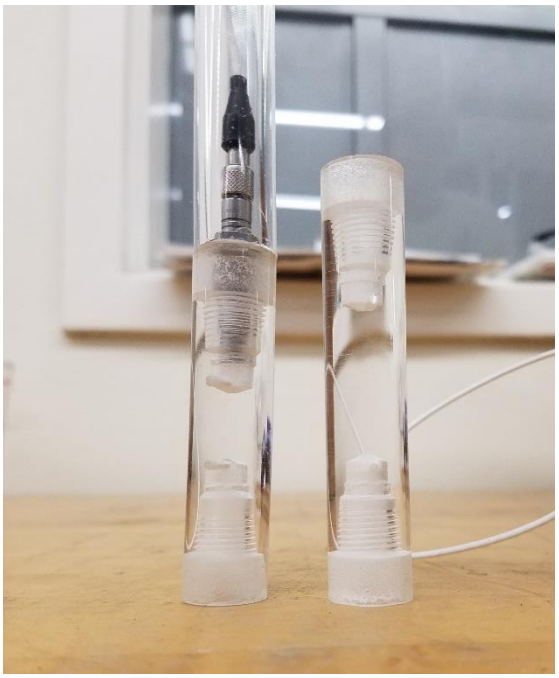

Figure 20. Dynamic pressure transducer fitted inside of a hollow acrylic rod

Implementation of the DPT's in this manner was successful. The DPT's were fed through hollow rods and screwed into a tapped acrylic rod. The 3 separate rod pieces were then sealed using a thin epoxy layer before painting and inserting into the test section. The tapped acrylic rod portion also contained a small hole allowing air to reach the DPT's. However data extraction from the DPT's during experimental testing yielded a couple issues. The first being that DPT's are not absolute pressure sensors, and cannot be used to accurately compare to the absolute pressures measured by PSP. The second issue that occurred was that the first facility used with BinaryFIB contained wind speeds slower than 20 m/s on the rods surface. This resulted in very little pressure differences reaching the DPT's and as a result most of the tests appeared to produce only noise.

Since the DPT's could not be accurately used for comparison a small secondary facility was constructed for the in-situ calibration.

The in-situ calibration was instead performed on a model test section of a single rod with static pressure transducers at evenly spaced locations along the rod. Pressure ports were centered along the top quarter of the rod surface. Wind speeds on the surface of the PSP rod and in-situ calibration model were measured using a hot film anemometer. The average wind speeds were matched between the two setups before sets of images were captured for analysis. The setup of the in-situ calibration can be seen in Figure 21.

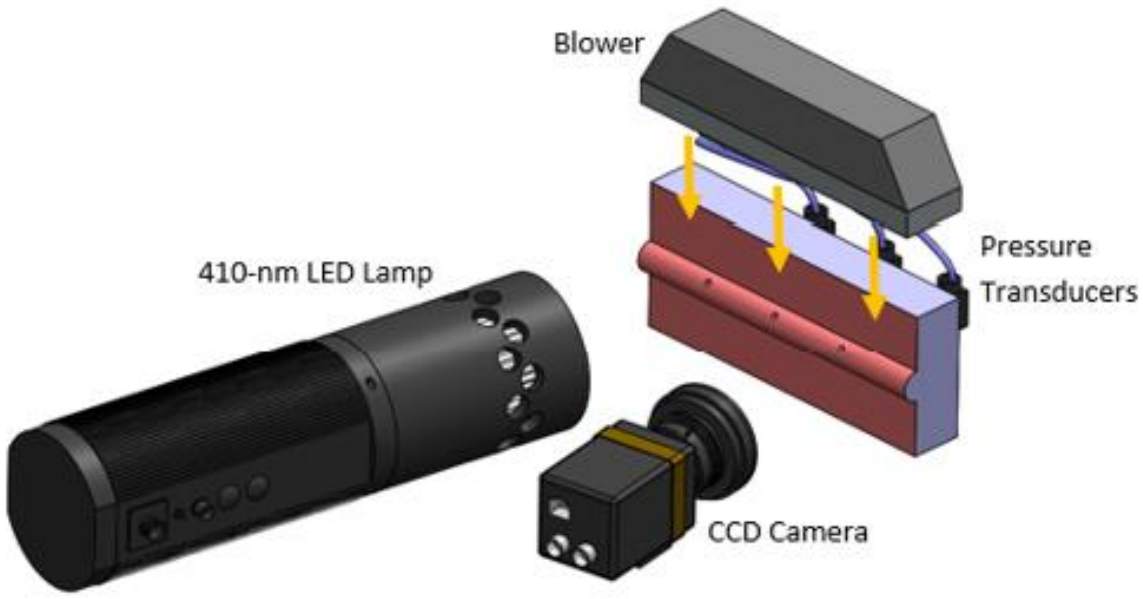

Figure 21. In-Situ calibration set-up

Experimental Method

The experimental setup within the test facility occurred as follows. Inlet velocity measurements were taken across a plane 0.13 m above the test section entrance. Measurements were taken using a hot film anemometer with an overall fluctuation no greater than 0.2 m/s. Experiments were done with an inlet velocity of V_{i1} = 3.8 m/s and V_{i2} =5.7 m/s corresponding to Re = 4000 and 6000, respectively. Figure 22 shows the CCD camera and 410-nm LED Lamp that were set up to capture the center region of the test section at the height of interest. The CCD camera captured images of 804 x 604 pixels. Each experimental test captured images at 3 fps for 100 images total. Due to the optical advantage, experiments focused on the outside-most outer bundle at Rods 8 and 10.

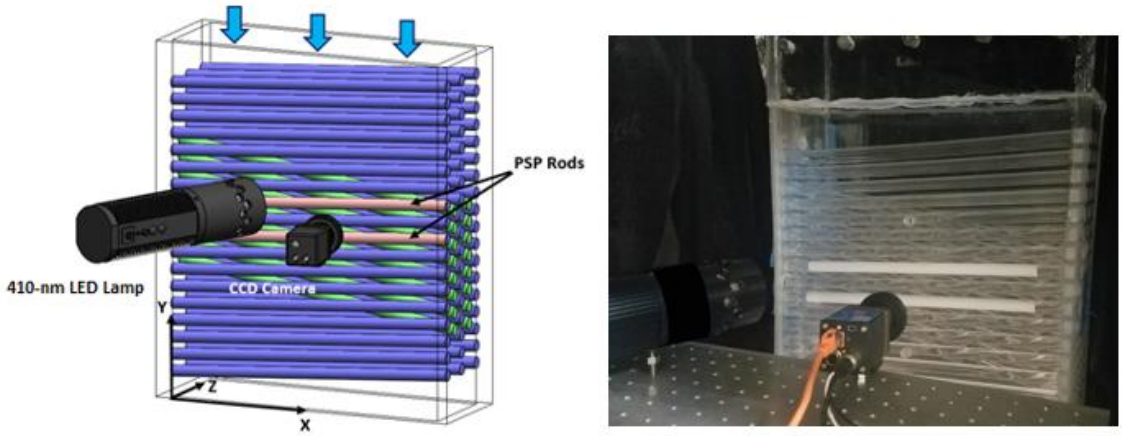

Figure 22. Experimental Set-up with PSP applied on Rods 8 and 10.

Rods 1 – 6 and Rods 15 – 18 of the outer bundle do not interact fully with adjacent tube bundles as a result of the geometry of the test section, therefore they were not considered for testing. Rods 8 and 10, chosen to measure the surface pressure on, have adjacent tube bundles. This region of interest is chosen due to the particular fluid behavior that previous studies have suggested incorporate the highest cross-flow turbulent behavior when looking at tube bundle geometry [7, 31]. Surface pressure measurements taken on Rods 8 and 10 were averaged for analysis. Average surface pressure was calculated using Equation 2.

$$\bar{P} = \frac{\sum P_{i,j}}{N} \qquad \text{Eqn. 2}$$

Average surface pressure, $\bar{P}$, is calculated by summing the pressures measured at each pixel in the image, P_{ij}, and dividing by the total number of pixels, N.

As mentioned in Chapter II, the facility was reconstructed for tests with fast PSP (TurboFIB). The purpose of the reconstruction was to provide higher inlet velocities to increase accuracy of measurements. TurboFIB calibrations and emission spectra are provided by the manufacturer and are shown below in Figure 23.

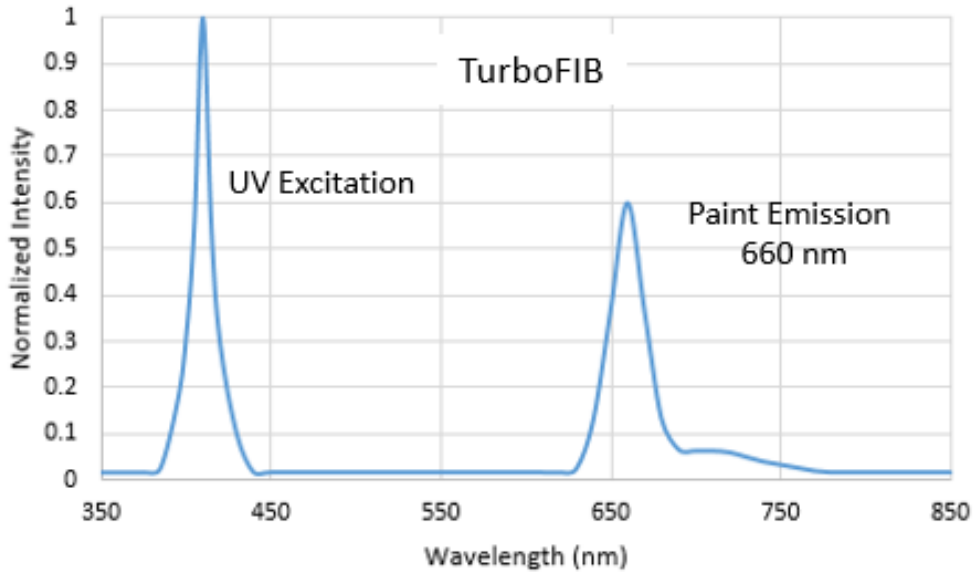

Figure 23. TurboFIB emission spectra

TurboFIB has a response time of less than 1 ms, 0.4% per ^{0}C temperature sensitivity, and 0.8% per kPa pressure sensitivity as reported by their manufacturer [35]. Experiments with TurboFIB used a CMOS camera instead of a CCD camera. A reflective filter was placed in front of a 610 nm filter to ensure only light at wavelengths above 610 nm were captured with the camera lens. An additional 410-nm LED lamp was also used. This is due to a need for more light since exposure must be higher to capture higher fps. The experimental setup for fast PSP is shown below in Figure 24.

Figure 24. Experimental set-up for TurboFIB

Experimental conditions for the tests were as follows. Inlet velocity measurements were taken across a plane 0.13 m above the test section entrance. Measurements were taken using a hot film anemometer with an overall fluctuation no greater than 0.2 m/s. Experiments were done with an average inlet velocity of V_i = 8.13 m/s and V_i = 11.09 m/s corresponding to Re = 8,500 and Re = 11,600, respectively. Due to the optical advantage, experiments focused on the outside-most outer bundle at Rods 8, 9, and 10. This region was chosen for the same considerations listed above that were used for BinaryFIB experiments.

CHAPTER IV

RESULTS AND ANALYSIS

Paint Thickness Calibration Results

Although pressure calibration curves are provided by the manufacturer, several pressure calibration tests were performed to verify the manufacturer's specifications, and to determine paint sensitivities to coat thickness. As mentioned previously in Chapter 3, a-priori tests were performed using BinaryFIB on rods in a sealed chamber. Rods were painted with varying paint coat thickness and pressurized with an air compressor. A raw wind-off image of BinaryFIB test procedure is captured and shown below in Figure 25. The raw image shown was used for the paint thickness sensitivity testing procedure. Results of both the a-priori and paint thickness sensitivity test are presented in Tables 1 and 2, respectively.

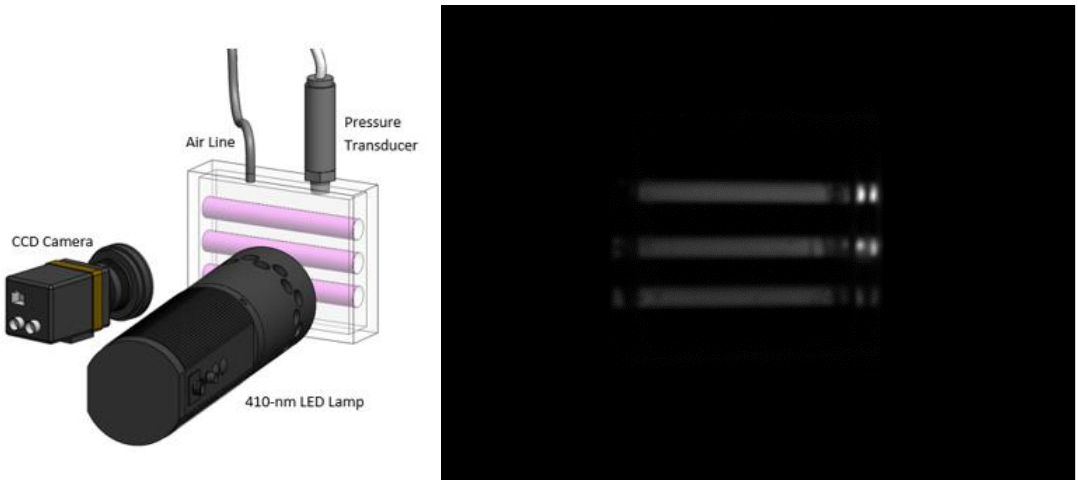

Figure 25. Raw image for paint thickness testing procedure

Table I. Results of paint thickness sensitivity testing.

Test Type	1	2	3	4	5
Pressure Transducer Reading (kPa)	164.00	173.24	196.61	231.57	259.15
Centerline Average (75 μm) (kPa)	170.76	180.68	205.64	240.25	268.87
Centerline Average (60 μm) (kPa)	170.41	180.96	206.33	239.84	267.56
Centerline Average (40 μm) (kPa)	171.86	182.55	208.47	244.87	275.35
Full Surface Average (75 μm) (kPa)	166.62	173.38	198.13	231.02	258.53

Table II. A-priori calibration results (paint thickness 75 μm)

Test No.	Pressure Transducer (kPa)	PSP (kPa)	% Difference
1	164.07	170.32	3.67
2	196.61	205.66	4.40
3	231.63	240.70	3.77
4	259.17	268.72	3.55

Comparison of surface averaged PSP readings to static pressure transducer readings show that PSP is accurate within 5% error at readings over 9 psi (163 kPa absolute). Centerline readings were significantly higher, implying that pressure readings over the rod were not all consistent, despite the pressure chamber being held at a static pressure. This may mean that due to the curvature of the rod, there might be additional uncertainties depending on location. However, the gauge pressures measured in this experiment were significantly higher than the pressures observed in facility testing, and ultimately these tests were used to determine optimal paint thickness. Paint thickness

was determined to be more accurate around 75 μm (9 cross coats of both base coat and PSP). Previous studies have shown paint thickness ranging from 50 μm to 200 μm provides consistent results [36].

In-situ Calibration Results

The in-situ calibration performed using BinaryFIB was used on the model shown in Figure 25. Wind speeds on the surface of the PSP rod within the model HCSG were measured to be an average of 20.6 m/s. The average wind-speed was matched within the in-situ calibration test section at 20.4 m/s. Sets of 100 images were taken for both wind off and wind on conditions. Wind speeds were matched based on speeds measured in the test section when Re = 4,000. Pressure transducers read an average of 101.4 kPa and the PSP measurements showed an average pressure of 101.8 kPa around the location of the port, corresponding to an absolute pressure difference of 0.4%. The in-situ calibration used a separate blower than the one used in the facility, and was not capable of matching speeds at higher Re.

A comparative study was done between the average pressure fields taken for Rod 8 at Re = 4,000. Similar to the in-situ calibration study that focused on the area around the pressure taps, an average pressure field was found for the top half of the rod. The average pressure on the top half of the rod at Re = 4,000 for the experiments within the model helical coil steam generator was 105.1 kPa. The difference between the pressures measured on the surface of the in-situ calibration and model HCSG was 8.7%. The difference between the gauge pressure measured by the PSP for the in-situ calibration

and the gauge pressure detected by the pressure transducers was 13.65%. As discussed by Liu and Sullivan [15], an in-situ calibration takes into account any systematic errors such as those with temperature effects and illumination variation by absorbing it into an overall fitting error. The uncertainty of the pressure sensitive paint measurements in this study is assumed to be equivalent to the difference between in-situ calibration and the pressure transducer measurements, 13.65% (gauge pressure), or 0.4% (absolute pressure).

The in-situ calibration for TurboFIB experiments was performed on the rods inside the test section, instead of on a model outside of the test section. The primary reason behind the discrepancy between the two in-situ calibration experiments was that it was found that pressures around the surface of a port on a hollow rod could be related to pressures inside the hollow rod when sealed. A hollow rod was machined to fit a static pressure transducer at the rod exit. The section of the hollow rod not connected directly to the static pressure transducer was sealed to prevent further pressure losses before reaching the static pressure transducer. The difference between the average surface pressure readings from the static pressure transducer and the surrounding pressure readings from the PSP yields the uncertainty. For Re = 8,500, the uncertainty is 10.1% and for the Re = 11,600, the uncertainty is 3.26%. An illustration of the setup is shown below in Figure 26. Additionally, results of all in-situ calibrations are summarized in Table III.

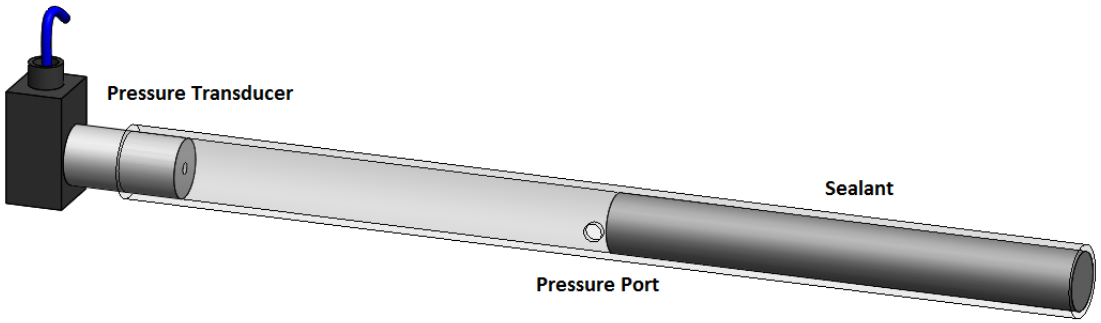

Figure 26. In-situ calibration for TurboFIB

Table III. Results of in-situ calibrations

Re	PSP (kPa)	Uncertainty (kPa)
4000	101.4	± 0.41
6000	102.40	± 0.41
8500	103.19	± 0.19
11600	103.41	± 0.07

Inlet Velocity Profile

For experiments with both BinaryFIB and TurboFIB, the inlet at the velocity was measured using a hot film anemometer. The purpose of inlet velocity measurements is to determine the Reynold's number and to determine areas in the facility with higher and lower velocities than average. The Reynold's number is calculated using Eqn. 3 below.

$$Re = \frac{V_i D}{\upsilon} \qquad \text{Eqn. 4}$$

Reynolds number is calculated using the average inlet velocity for V_i, kinematic viscosity calculated using the average temperature for ν, and rod diameter for D. The rod

diameter is used as characteristic length for each set of tests. Inlet velocities were measured at points in an inlet placed directly on top of the test section. Velocities were measured using a hot film anemometer that was placed at points 1 and 2 at locations A-E as shown in Figure 27 below. At each point 30 seconds of data was collected. The averages of points 1 and 2 are presented for each test presented, and are shown in Table IV.

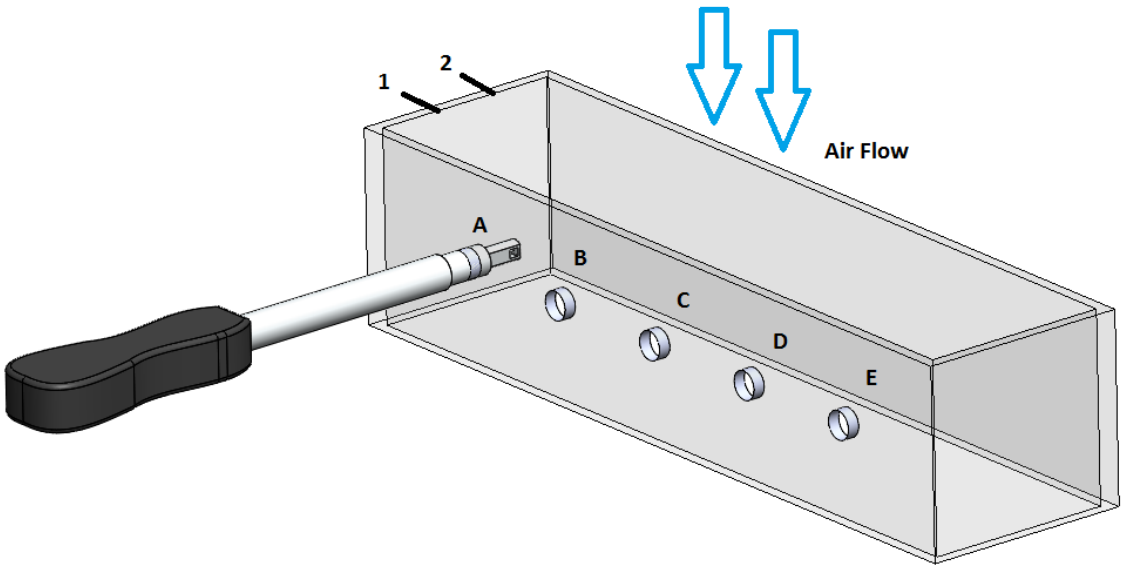

Figure 27. Inlet velocity measurements using hot film anemometer

TABLE IV. Velocity Profiles

Test No.	A	B	C	D	E	Average	Re
1	3.58	3.68	3.71	3.87	3.58	3.68	4,000
2	5.35	5.63	5.66	5.91	5.58	5.63	6,000
3	4.09	8.28	9.49	9.46	9.33	8.13	8,500
4	5.65	11.72	12.98	13.00	12.75	11.22	11,600

Sensitivity Tests

Analysis of pressure fields from PSP experiments typically involves applying a smoothing kernel. The purpose of the smoothing kernel is to improve signal-to-noise ratio, and to help clarify pressure field visualization. To determine the smoothing kernel size, a sensitivity study was performed. The sensitivity study was performed by analyzing the surface pressure average as a function of kernel size. Optimal kernel size was chosen based upon when the average pressure values on the rod converged. Convergence was determined by using a method outlined by S. Lee, which is commonly used in CFD [16]. In this type of test, a residual is calculated as the difference between images n and n-1. The residual is calculated using Eqn. 5.

$$R_{PSP}(n)\% = \frac{(P_{i,j}^{n} - P_{i,j}^{n-1})}{P_{i,j}^{n-1}} \times 100 \qquad \text{Eqn. 5}$$

Where R_{PSP} is the residual value, $P_{i,j}^{n}$ is the averaged pressure at (i,j) of the batch containing n number of images, $P_{i,j}^{n-1}$ is the averaged pressure at (i,j) of the previous batch containing n-1 number of images.

The residual for the Gaussian smoothing factor was calculated for tests using BinaryFIB and TurboFIB. The residual was determined to reach convergence when R_{PSP} is < 2%. For BinaryFIB experiments, the kernel size converged at a smoothing factor of 8×8, and for TurboFIB experiments the kernel size converged at a smoothing factor of 12×12. Results of the Gaussian smoothing factor sensitivity tests for Binary FIB and Turbo FIB are shown below in Figures 28 and 29, respectively.

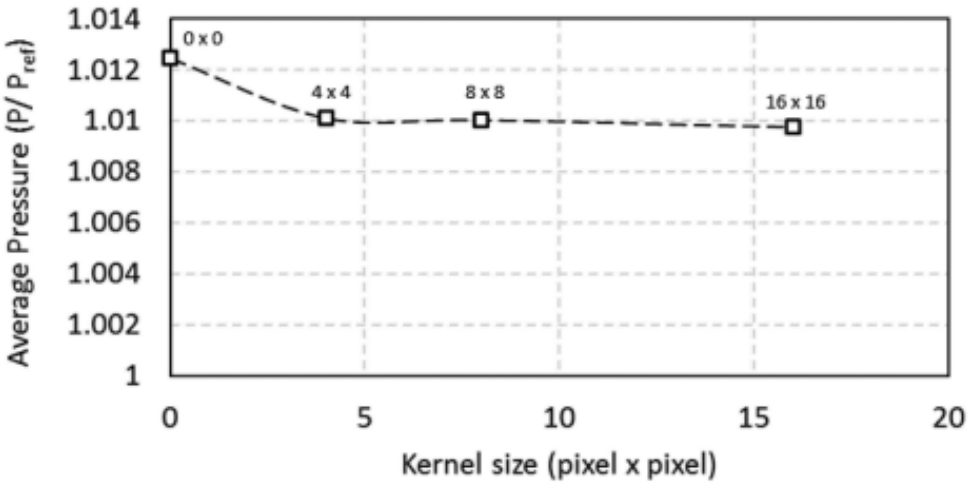

Figure 28. Average pressure as a function of kernel size for BinaryFIB tests.

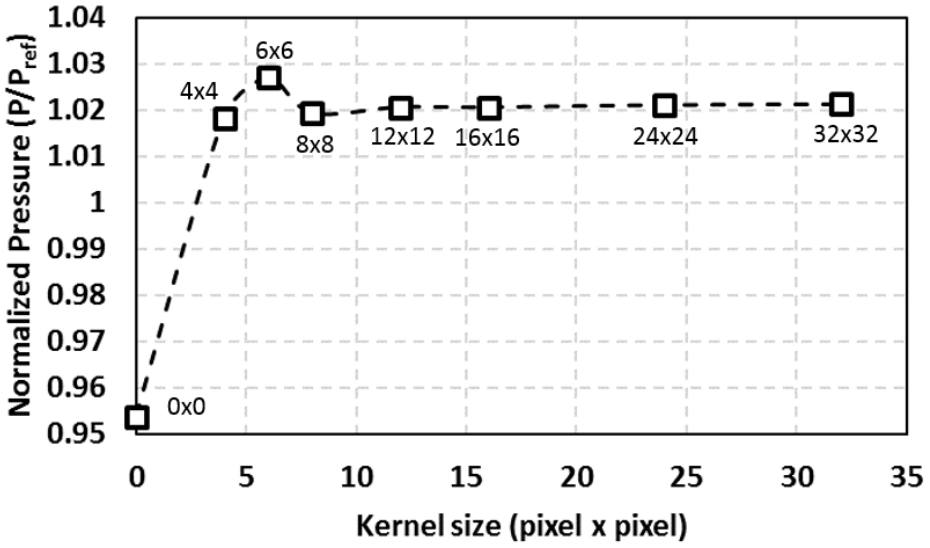

Figure 29. Average pressure as a function of kernel size for TurboFIB tests.

Figure 28 shows that for kernel filters larger than 4×4, average pressure is not fluctuating; therefore there are several options for selection kernel size for images. For

BinaryFIB experiments, a 16×16 kernel size was used for all results, as it provides minimal statistical changes in average pressure, and provides a clear representation of pressure fields. Figure 29 shows that for kernel filter sizes larger than 12×12, average pressures are not fluctuating. For TurboFIB experiments, a 12×12 filter size was chosen, since the image quality was already clear due to the improved resolution from using a CMOS camera. An example of image quality difference is shown below in Figure 30.

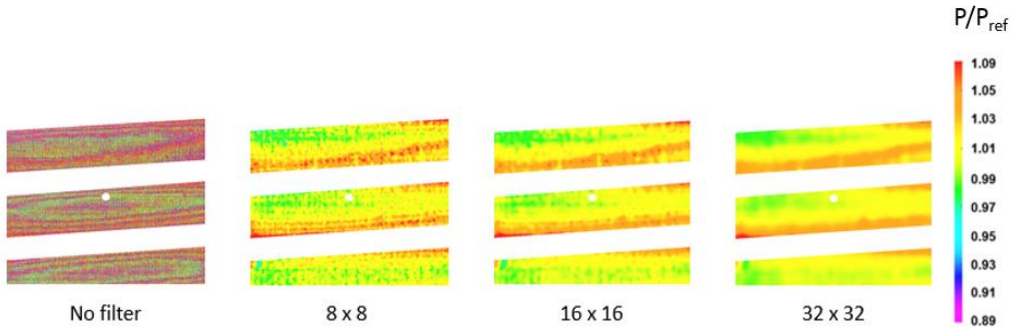

Figure 30. Visual change in images based on Gaussian smoothing kernel (TurboFIB)

To determine the number of images that need to be averaged to reach a statistical average, the same convergence approach is used. The residual is considered to be converged when R_{PSP} is < 2%.

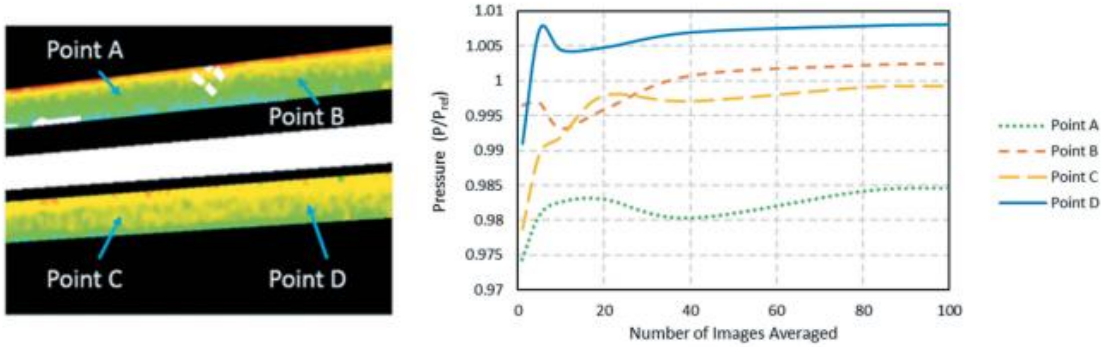

Figure 31. Pressure as a function of images averaged, BinaryFIB.

The residual is calculated at four points within the analysis area. The points A, B, C, and D are shown in Figure 31. Points were chosen at the center points of each rod at points along that x-axis that correspond to lengths one-quarter and three-quarters along the full length of the image. These points were selected due to their distance from each other, and because the pressure fluctuations between frames was more consistent than on the rods edge. The residual is determined to reach convergence when R_{PSP} is < 2% change. For BinaryFIB tests, convergence is reached when more than 90 images are averaged.

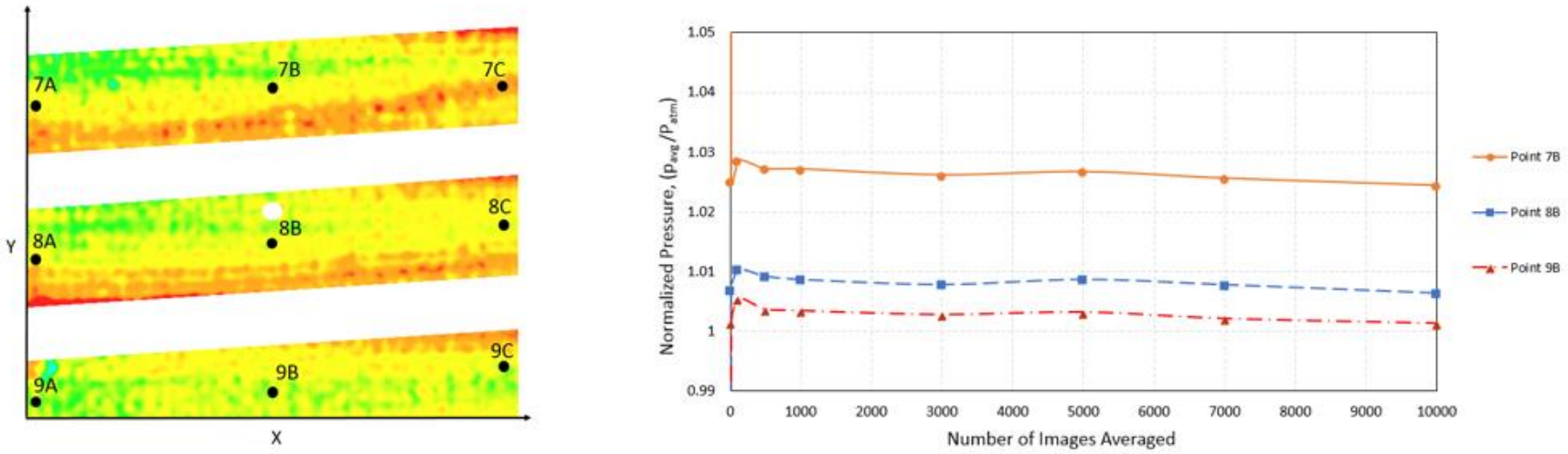

Figure 32. Pressure as a function of images averaged, TurboFIB

The residual was also calculated at nine points on the rods for the analysis area of the TurboFIB PSP. The points 7A-9C are shown in Figure 32. Points were chosen at locations to with both higher and lower pressure fluctuations, and were spread out to ensure a statistical average would represent the analysis area. The residual is determined to reach convergence when R_{PSP} is < 2%. For TurboFIB experiments, convergence is reached when more than 1,000 images are averaged.

Experimental Results

Figure 33 shows an example of a BinaryFIB "wind-off" image captured by the camera when there was no air through the wind tunnel. Rods 7, 9, 11, and 12 were subtracted out of the image for visual clarity. The following results focus on Rods 8 and 10 that were coated with PSP.

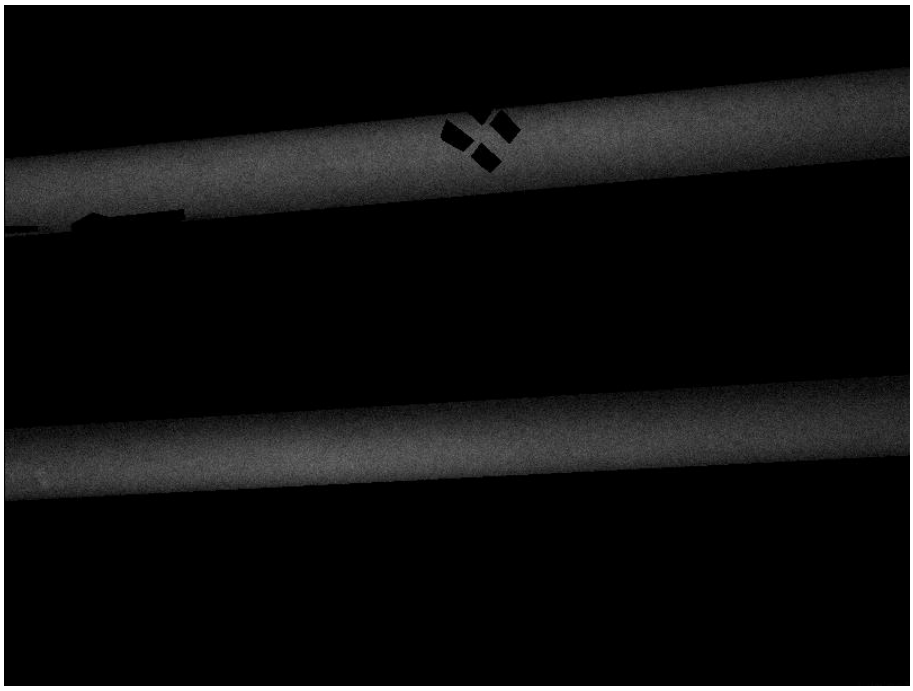

Figure 33. Background subtracted wind-off image (BinaryFIB)

Figure 34 shows an example of a background subtracted TurboFIB “wind-off” image captured by the camera when there was no air through the wind tunnel. The following results focus on Rods 8, 9, and 10 that were coated with PSP.

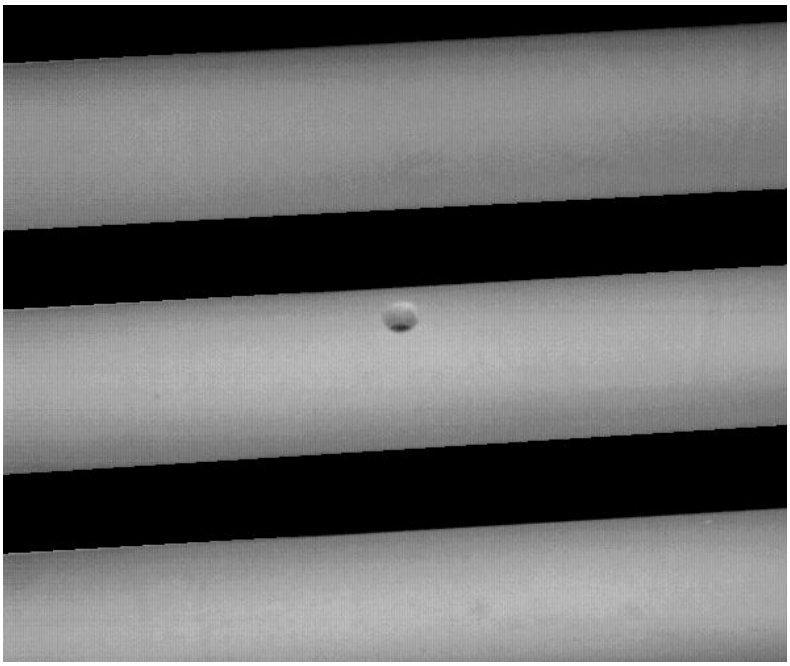

Figure 34. Background subtracted wind-off image (TurboFIB)

Both BinaryFIB and TurboFIB experiments used OMSLite^{TM} (ISSI Inc.) for image processing and analysis. Images were averaged for surface pressure analysis based upon the results of sensitivity testing. For BinaryFIB images, a corrected wind-on image was created due to optical distortions. Light reflections and scratches in the paint were subtracted from the image. These corrections are present on images taken for analysis for both Re 4,000 and 6,000. For TurboFIB images, several distortions were present in the wind-off and wind-on images. These corrections were made to both sets of images by cropping the images to a smaller analysis area. They were applied to all images taken for analysis. As a result of image cropping, only part of Rod 9 is visible in the analysis.

Instantaneous Surface Pressure Field Measurements

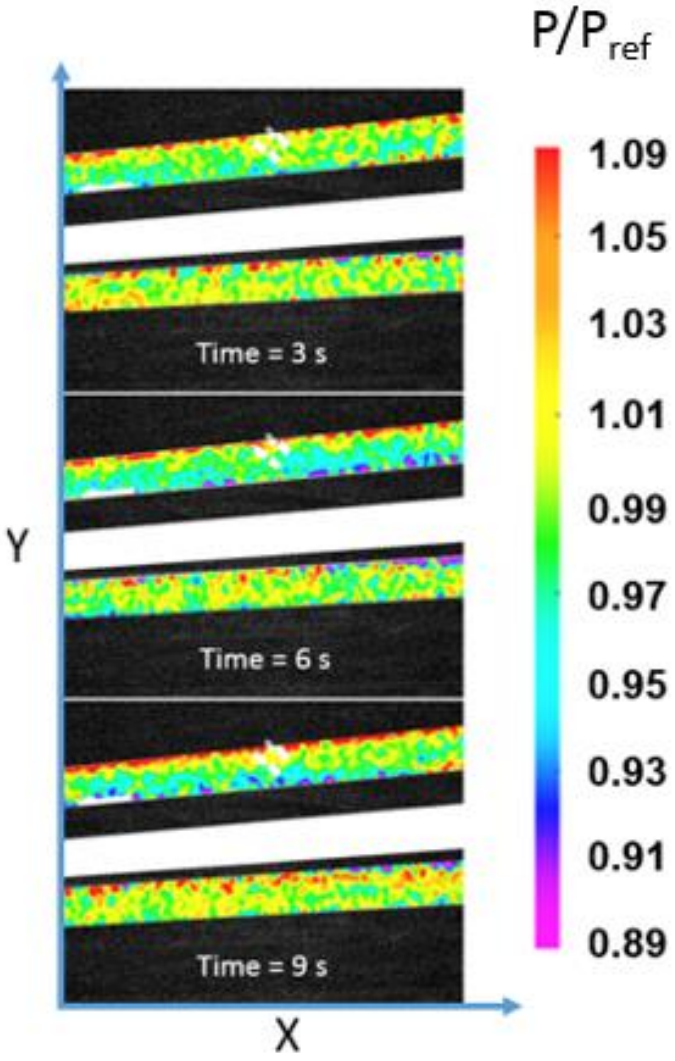

Figure 35. Select instantaneous pressure measurements using PSP on the surface of the rods at Re = 6,000

Pressure field measurements done with pressure sensitive paint at low speeds depends on averaging to reduce errors in oxygen quenching variations [28]. Experiments conducted found the variation in pressure that the pressure sensitive paint on a rod experienced within the heat exchanger geometry. An example of the variation of pressure on the rods is seen in Figure 35. At three interval time steps, the instantaneous pressure on the surface of Rods 8 and 10 show similar trends with different localized pressure magnitudes. Additionally, pressures are found to be significantly higher on the top portion of the rods. As mentioned previously, pressure fields at low speeds will have better accuracy when averaged over a period. At 3 fps, 100 images were captured for tests at Re 4,000 and 6,000.

The average pressure difference between the rods was 0.18 kPa. The average pressure and standard deviation between instantaneous frames for Rod 8 was 101.89 kPa and 0.61 kPa, respectively. The average pressure and standard deviation between instantaneous frames for Rod 10 was 101.71 kPa and 0.73 kPa, respectively. Average surface pressure measurements were found to be similar at each time measured for both rods. To elaborate, when the pressure on Rod 8 is found to be higher than average, the pressure on Rod 10 is typically also higher than average. Rod 10 was measured to have a larger standard deviation and variance than Rod 8, despite having a lower average surface pressure.

Averaged Surface Pressure Field Measurements

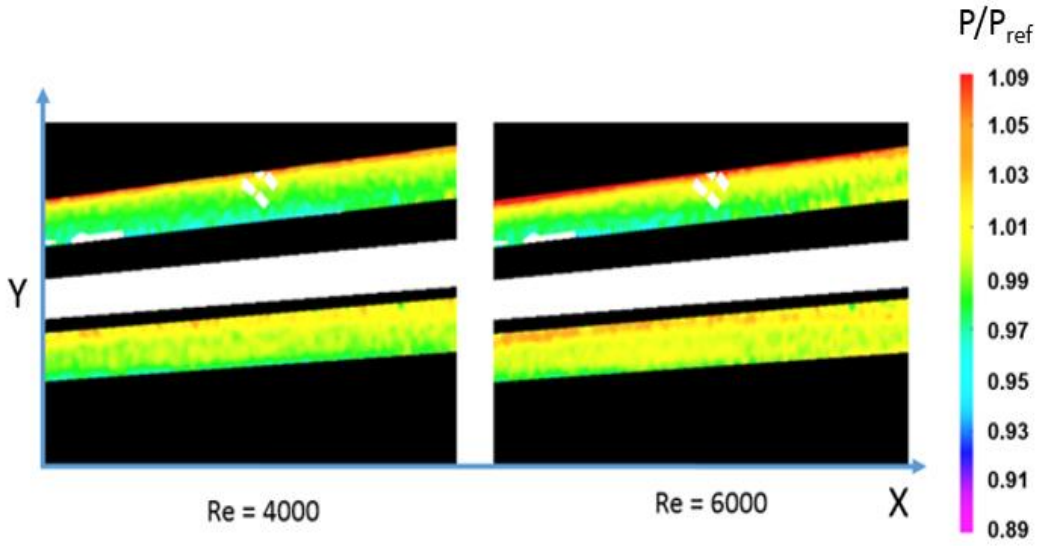

Figure 36. Normalized pressure fields for tests taken at Re = 4,000 and Re = 6,000

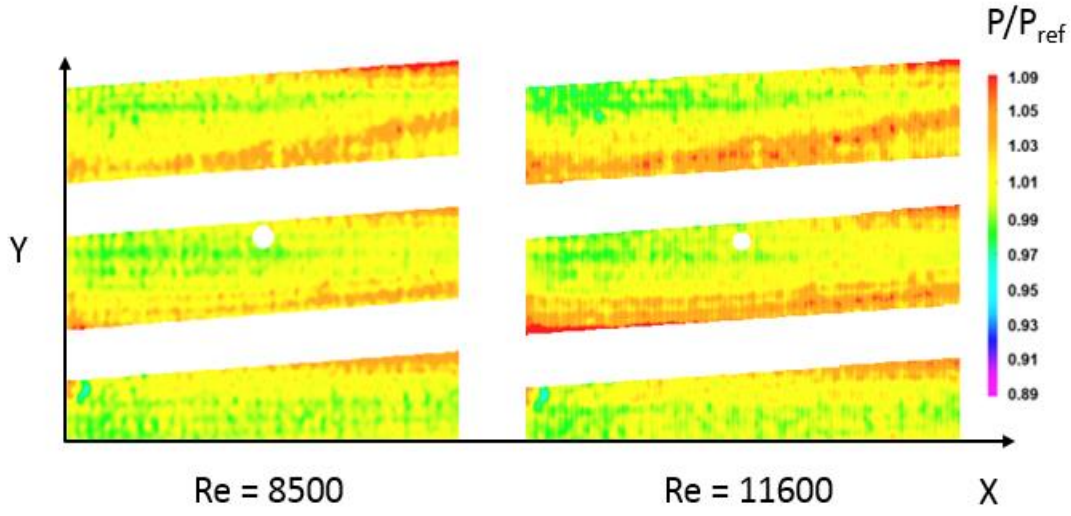

Figure 37. Normalized Pressure fields for tests taken at Re = 8,500 and Re = 11,600

As expected, average surface pressure across the rods is significantly higher on as Reynolds Number increases. As shown in Figures 36 and 37, pressure fields measured at Re 4,000 and 6,000 show the rods have higher pressures above the center portions of the rod, while pressure fields measured at Re = 8,500 and Re = 11,600 show high pressures detecting on the lower half of the rods.

The average surface pressure and standard deviation for Rod 8 were 101.4 kPa and 2.6 kPa for Re = 4,000, and 102.4 kPa and 3.3 kPa for Re = 6,000, respectively. The average surface pressure and standard deviation for Rod 10 were 101.9 kPa and 1.4 kPa for Re = 4,000, and 102.7 kPa and 1.4 kPa for Re = 6,000. Uncertainty for all average surface pressure readings is calculated to be within ± 0.41 kPa. The average surface pressure was measured to be significantly higher for Re = 6,000 than the average surface pressure of the 100 instantaneous frames.

The average surface pressure on all rods under Re = 8,500 was found to be 103.19 kPa with a standard deviation of 1.68 kPa. The average pressure on all rods under Re = 11,600 was found to be 103.41 kPa with a standard deviation of 2.05 kPa. The average surface pressure within a 10 pixel radius outside the port was 101.91 kPa for Re = 8,500 with a standard deviation of 1.04 kPa, and 101.95 kPa for Re = 11,600 with a standard deviation of 0.82 kPa.

During testing, a static a pressure transducer was placed inside the end of Rod 9 (hollow rod) and measured 101.358 kPa and 101.456 kPa corresponding to Re = 8,500 and 11,600, respectively.

Surface Pressure distributions were determined at selected profiles listed in Table V and shown on Figure 38. Profiles were chosen at a variety of different lateral pitch ratios to determine if there were any patterns between the lateral pitch ratio and the pressure fields.

Table V. Lateral pitch ratio along each line

Location	Lateral Pitch Ratio
Line A	0.00
Line B	0.24
Line C	0.49
Line D	0.74
Line E	0.98
Line F	1.24
Line G	0.00

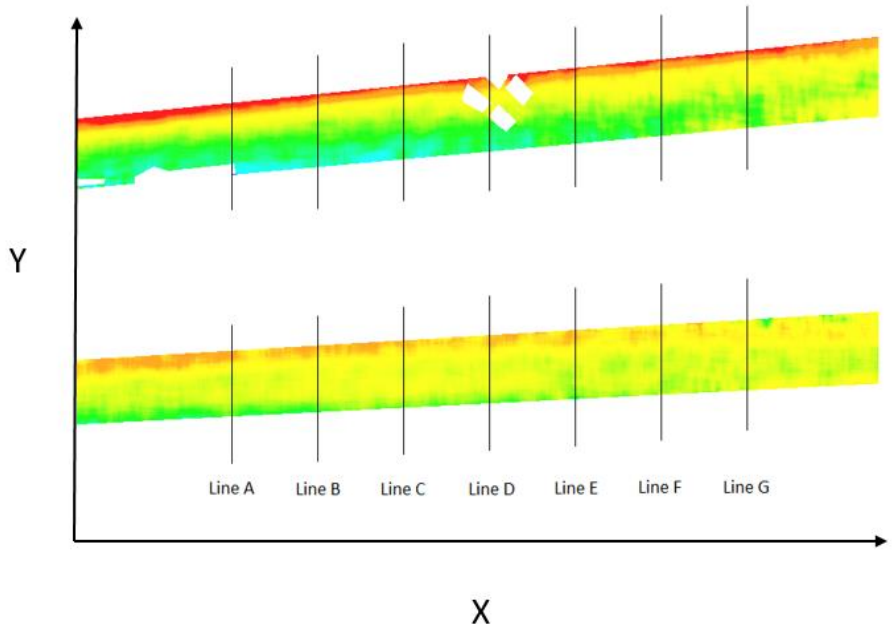

Figure 38. Location of lines A-G

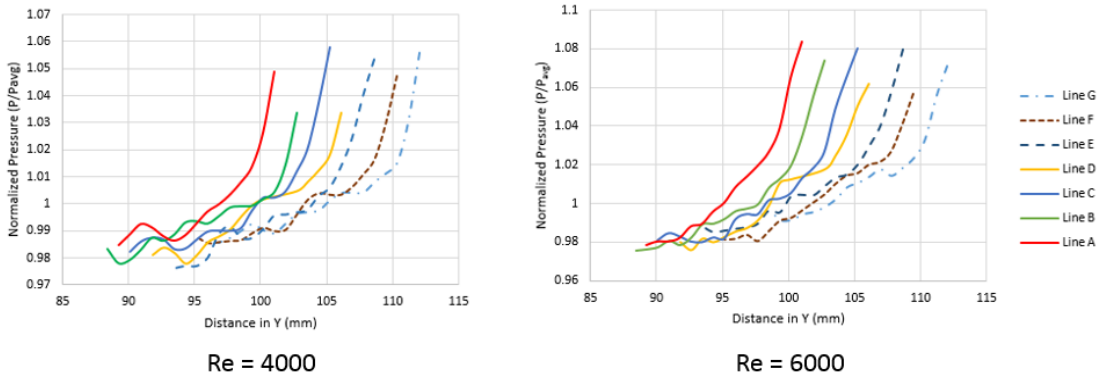

Figure 39. Pressure distributions along Rod 8

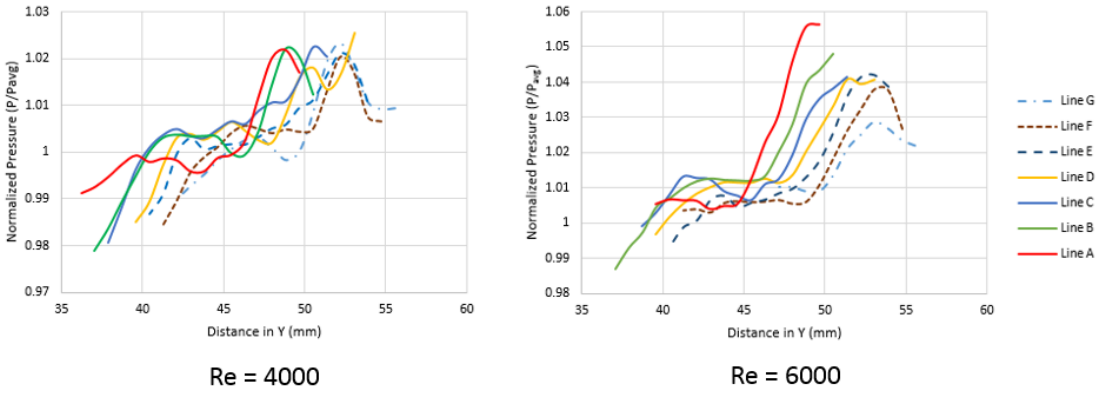

Figure 40. Pressure Distributions along Rod 10

Surface pressure distributions measured using BinaryPSP at Re= 4,000 and 6,000 are shown in Figures 39 and 40, and were found to have no discernible patterns between lateral pitch ratio and pressure distribution along the rod. Instead, pressure distributions were found to share similarities based upon rod placement within the model. This could

be due to flow being more or less developed between certain tube layers, or caused by turbulence from flow phenomena such as vortex shedding, which is known to occur more rapidly in geometries with interlacing tube bundles.

As mentioned in Chapter I, previous studies used the non-dimensional parameter C_p to describe the pressure coefficient and compare pressure distributions found circumferentially around rods. Figure 41 shows C_p for Rod 8 at Re 4,000, 6,000, 8,500, and 11,600 when the lateral pitch ratio, a, is 0 or the cross section is in-line.

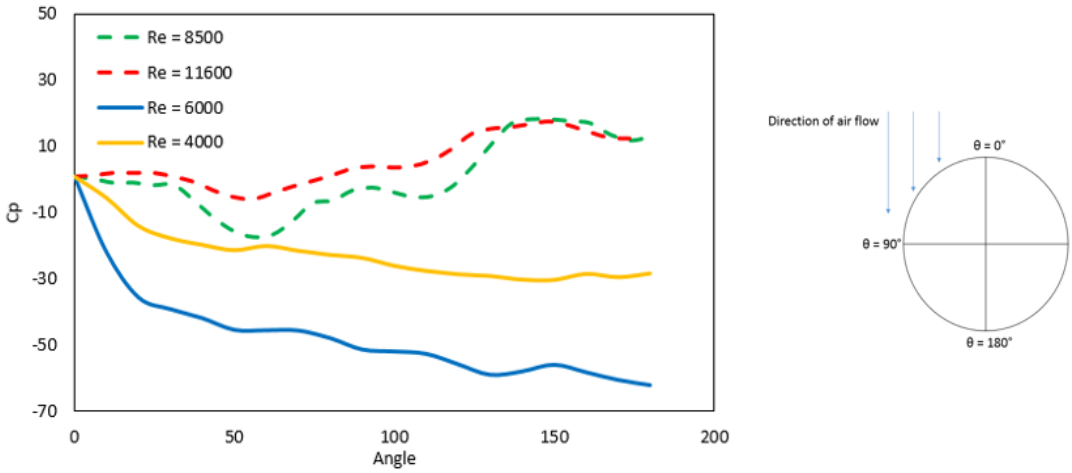

Figure 41. Pressure coefficient around Rod 8 at Re = 4000, 6000, 8500, 11600

The pressure coefficient distributions shown in Figure 41 do not have similarities beyond sharing similar curves shapes for each respective test, i.e. the BinaryFIB experiments have the same curvature. At Re = 4,000 and 6,000 the pressure coefficient

distribution is similar to those found in previous literature, but the distributions at Re = 8,500 and 11,600 do not share similarities [22].

CHAPTER V
SUMMARY AND CONCLUSION

Summary

HCSG's are tube and shell heat exchanger designs proposed for use in the nuclear industry. They offer improved heat transfer efficiencies, but the design of these heat exchangers depends upon their cross sections between tube bundles, which greatly affects the cross flow between the tubes. A facility was constructed to study a HCSG design containing interlacing tube bundles using PSP to measure pressure on the surface of rods. PSP is an optical measurement technique that uses the principle of oxygen quenching and fluorescent dyes to determine pressure on the surface of an object. The technique is non-invasive and can provide much higher spatial resolutions than standard pressure transducer measurements, without obstructing the flow. Two different paint formulations, BinaryFIB and TurboFIB, were used in this study. BinaryFIB experiments were captured using a CCD camera with a single LED lamp. TurboFIB experiments were captured using a CMOS camera with two LED lamps to increase the exposure for image collection at higher speeds.

Experiments captured images of near-wall rods under Re 4000, 6000, 8500, and 11600. Calibration tests were performed prior to experiments to determine optimal paint thickness and uncertainty in pressure measurements. Calibration results determined paint thickness in the range of 60 to 200 μm provides consistent results, 75 μm was used for experiments to account for human error in painting and to prevent wasteful use of paint. Uncertainty in PSP measurements was determined by in-situ calibrations. In-situ

calibrations compare paint measurements to pressure transducer measurements within a model or test facility. Uncertainty was found to depend on the Re of the flow the paint is in, but ranges from 3.26% at Re 11600 to 13.65% at Re 4000.

Conclusions

Instantaneous measurements using PSP were found to have significant uncertainties due to the signal-to-noise ratio being too low. PSP cannot accurately provide resolved results for low wind-speed flows without additional analysis, as the paint has a low pressure sensitivity. Uncertainty in pressure readings can be reduced by increasing the wind speeds to ensure pressure sensitivity is not a factor, or by averaging images to reach a statistical average. Additionally, other methods are being developed to use PSP in low wind speed flows, such as proper orthogonal decomposition [29].

Surface pressure distributions were measured along Lines A-G for BinaryFIB experiments. Patterns were not visible between lateral pitch ratio and pressure distribution. However, pressure distributions along the same rods had similar patterns. Pressure readings on Rods 9 and 10 were more erratic across the rod laterally, which could be caused by an increase in turbulence beneath Rod 8. The second column of tubes begins forming the shifting cross section beneath Rod 8, which may result in increased turbulence. The shifting cross section in the tube bundle may affect the rate at which vortex shedding is occurring. An increased rate of vortex shedding would have profound effects on the pressure distributions observed on the rods, and this could be causing the discrepancies between the pressures on the rods [3, 15, 37-39]. Currently, flow

phenomena in changing tube bundle arrangements is not well understood, and significant research remains to be done on these arrangements.

Pressure coefficient distributions were taken at points where the cross section is inline. There were similarities in the shape of the pressure coefficient distribution found between Re 4000 and 6000, and Re 8500 and 11600. However, the Re 8500 and 11600 shared no similarities with the Re 4000 and 6000 tests. This implies the cross section has limited effect on the pressure coefficient, and turbulence caused by an increase in Re is a more significant factor. Distributions at Re 4000 and 6000 were found to match those measured in previous literature [22]. Ultimately, the results of this study do not match what has been predicted by previous correlations for staggered and in-line tube bundles, and may be representative that there is a need for a geometric sensitivity study in shifting tube bundle arrangements.

REFERENCES

1. IAEA, Advances In Small Modular Reactor Technology Developments, International Atomic Energy Agency, Vienna Austria, 2018.
2. D. G. Prabhanjan, V.G.S. Raghavan, T.J. Rennie, "Comparison of heat transfer rates between a straight tube heat exchanger and a helically coiled heat exchanger" *International Communications in Heat and Mass Transfer,* Vol. 29, (2002) pp. 185-191. DOI: 10.1016/S0735-1933(02)00309-3
3. A. Zukauskas, R. Ulinkskas, "*Heat Transfer in Tube Banks in Crossflow,*" Hemisphere Publishing Corporation, New York, (1988).
4. J. P. Holman, "*Heat Transfer,*" McGraw-Hill, New York, (1990). DOI: 10.1002/aic.690180643
5. W. M. Kays, A. L. London, "*Compact Heat Exchangers,*" The National Press, Palo Alto, (1955).
6. H. Martin, V. Gnielinski, "Calculation of Heat Transfer from Pressure Drop in Tube Bundles," *3rd European Thermal Sciences Conference*, (2000). DOI: 10.1021/ie50324a027
7. S.B. Beale, D.B. Spalding, A numerical study of unsteady fluid flow in in-line and staggered tube banks, J. Fluids Struct., **13,** (2011). DOI: 10.1006/jlfs.1999.0231
8. IAEA, Innovative Small and Medium Sized Reactors: Design Features, Safety Approaches and R&D Trends, Tech. Rep. IAEA-TECDOC-1451, International Atomic Energy Agency, Vienna Austria, 2005.

9. M. Esch, A. Hurtado, D. Knoche, W. Tietsch, "Analysis of Steam Outlet Temperatures of helical Coil Steam Generators for HTRs with the System Code TRACE" *Proceedings of HTR 2010,* (2010). DOI: 10.1016/j.nucengdes.2011.09.056

10. E.K. Kim, and S.O. Kim, "Sodium-Cooled Fast Reactor Helical Coil Steam Generator," *Transactions of the Korean Nuclear Society Autumn Meeting*, Jeju, Korea, October 21-22, 2010, pp.47 (2010).

11. Xin, R.C., Awwad, A., Dong, Z. F., and Ebadin, M. A., "An Investigation and Comparative Study of the Pressure Drop in Air-Water Two-Phase Flow in Vertical Helicoidal Pipes" *International Journal of Heat and Mass Transfer*, vol. 39, no. 4, pp. 735-743, 1996. DOI: 10.1016/0017-9310(95)00164-6

12. Ali, M. A., "Natural Convection Heat Transfer From Vertical Helical Coils in Oil" *Heat Transfer Engineering*, vol. 27, no. 3, pp. 79-85, 2006. DOI: 10.1080/01457630500458617

13. Futugami, K., and Aoyama, Y., "Laminar Heat Transfer in Helically Coiled Tubes" *International Journal of Heat and Mass Transfer*, vol. 30, no. 3, pp. 207-220, 2009. DOI: 10.1016/0017-9310(88)90021-X

14. Merzari, E., Yuan, H., Kraus, A., Obabko, P., Fischer, P., Solberg, J., Lee, S., Lai, J., Delgado, M., and Hassan, Y. A., "High-Fidelity Simulation of Flow-Induced Vibrations in Helical Steam Generators for Small Modular Reactors" *Nuclear Technology*, Vol. 205, pp. 33-47, 2019. DOI: 10.1080/00295450.2018.1490124

15. E. E. Konstantinidis, S. Balabani, M. Yianneskis, “A Study of Vortex Shedding in a Staggered Tube Array for Steady and Pulsating Cross-Flow,” ASME. *J. Fluids Eng.* **124**, (2002) pp.737-746. DOI:10.1115/1.1487359.

16. S. Lee, M. Delgado, S. J. Lee, and Y. A. Hassan. "Experimental investigation of the isothermal flow field across slant 5-tube bundles in helically coiled steam generator geometry using PIV." *Nuclear Engineering and Design*, vol. 338, 2018. DOI: 10.1016/j.nucengdes.2018.08.012

17. P. Batham, Pressure Distribution on in-line tube arrays in cross flow, International Symposium on Vibration Problems in Industry, Keswick, U.K Paper No. 411, pp. 1-24 (1973).

18. M. M. Zdravkovich, and J.E. Namork, Excitation, amplification, and suppression of flow-induced vibration in heat exchangers, Practical Experiences with Flow Induced Vibration, Paper A5, pp. 107 – 117 (1980).

19. J. Buxmann, Pressure Losses in Tube Bundles of Close Spacings, Design and Operation of Heat Exchangers, W. Roetzel et al. Berlin: Springer (1991).

20. L. Ljungkrona, and B. Sunden, “Flow Visualization and Surface Pressure Measurement on Two Tube in an Inline Arrangement,” Experimental Thermal and Fluid Science, 6, pp. 15 – 27 (1993). DOI: 10.1016/0894-1777(93)90037-J

21. J. Mahon and C. Meskell, “Surface Pressure Distribution Survey in Normal Triangular Tube Arrays,” Journal of Fluids and Structures, 25 pp. 1348 – 1368 (2009). DOI: 10.1016/j.jfluidstructs.2009.07.006

22. J. Mahon and C. Meskell, “Surface Pressure Survey in a Parallel Triangular Tube Array,” Journal of Fluids and Structures, 34, pp. 123 – 137, (2012). DOI: 10.1016/j.jfluidstructs.2012.05.005

23. D.B. Keogh and C. Meskell, “Bi-stable Flow in Parallel Triangular Tube Arrays with a Pitch-to-Diameter Ratio of 1.375,” Nuclear Engineering and Design, 285, pp. 98-108 (2015). DOI: 10.1016/j.nucengdes.2015.01.009

24. A. Khalifa, D. Weaver, S. Ziada, “Modeling of the phase lag causing fluidelastic instability in a parallel triangular tube array,” Journal of Fluids and Structures, 43, pp. 371-384 (2013). DOI: 10.1016/j.jfluidstructs.2013.09.014

25. B. de Pedro, J. Parrondo, C. Meskell, J.F. Oro, “CFD modelling of the cross-flow through normal triangular tube arrays with one tube undergoing forced vibrations or fluidelastic instability,” Journal of Fluids and Structures, 64, pp. 67 – 86 (2016). DOI: 10.1016/j.jfluidstructs.2016.04.006

26. J. Peterson and R. Fitzgerald, “New technique of surface flow visualization based on oxygen quenching of fluorescence” *Review of Scientific Instruments,* Vol. 51, (1980) pp. 670-671. DOI: 10.1063/1.1136277

27. T. Liu and J.P. Sullivan, *Pressure and Temperature Sensitive Paints,* Springer, Berlin, Germany (2005). DOI: 10.1002/9780470686652.eae076

28. R. H. Engler, M.C. Mérienne, C. Klein, Y. Le Sant, “Application of PSP in low speed flows” *Aerospace Science and Technology,* Vol. 6, (2002) pp. 313-322. DOI: 10.1016/S1270-9638(02)01168-9

29. D. Peng, S. Wang, Y. Liu, “Fast PSP measurements of wall-pressure fluctuation in low-speed flows: improvements using proper orthogonal decomposition” *Experiments in Fluids*, **57**, (2016) pp. 1-17. DOI: 10.1007/s00348-016-2130-z

30. L. Yang, H. Zare-Behtash, E. Erdem, K. Kontis, “Application of AA-PSP to hypersonic flows: The double ramp model” *Sensors and Actuators*, Vol. 161, (2012) pp. 100-107. DOI: 10.1016/j.snb.2011.09.053

31. M. E. Sellers, M. A. Nelson, J. W. Crafton, “Dynamic Pressure Sensitive Paint Demonstration in the AEDC Propulsion Wind Tunnel 16T*” American Institute of Aeronautics and Astronautics, (2016). DOI: 10.2514/6.2016-1146

32. J. N. Reyes Jr., “NuScale Plant Safety in Response to Extreme Events,” *Nuclear Technology*, **178**, pp. 153-163 (2017). DOI: 10.13182/NT12-A13556

33. N. V. Hoffer, P. Sabharwall, N. A. Anderson, Modeling a Helical-coil Steam Generator in RELAP5-3D for the Next Generation Nuclear Plant, INL/EXT-10-19621, Idaho National Laboratory, Idaho Falls Idaho, 2011.

34. R. D. Mehta, and P. Bradshaw. “Design Rules for Small Low Speed Wind Tunnels.” The Aeronautical Journal (1968), vol. 83, no. 827, pp. 443–453 (1979). doi:10.1017/S0001924000031985.

35. “TurboFIB Pressure Sensitive Paint,” Innovative Scientific Solutions, Inc. 2020. URL: https://innssi.com/fast-pressure-sensitive-paints/

36. T. Hayashi and H. Sakaue, “Dynamic and Steady Characteristics of Polymer-Ceramic Pressure-Sensitive Paint with Variation in Layer Thickness” *Sensors*, **17**, (2017) pp. 1-9. DOI: 10.3390/s17051125

37. S.S. Paul, M.F. Tachie, S.J. Ormiston, Experimental study of turbulent cross-flow in a staggered tube bundle using particle image velocimetry, Int. J. Heat Fluid Flow, **28,** (2007) pp.441-453. DOI: 10.1016/j.ijheatfluidflow.2006.06.001

38. S. Lee, Y. A. Hassan, “Experimental study of flow structures near the merging point of two parallel plane jets using PIV and POD” *International Journal of Heat and Mass Transfer*. **116**, (2018) pp. 871-888. DOI: 10.1016/j.ijheatmasstransfer.2017.09.047.

39. C. Iwaki, K.H. Cheong, H. Monji, G. Matsui, PIV Measurement of the vertical cross-flow structure over tube bundles, Exp. Fluids, **37,** (2004) pp.350-363. DOI: 10.1007/s00348-004-0823-1